

2022-05-01

## Suitability of Low-Cost Additive Manufacturing for Polymer Electrolyte Fuel Cells

David Alexander  
*The University of Texas at El Paso*

Follow this and additional works at: [https://scholarworks.utep.edu/open\\_etd](https://scholarworks.utep.edu/open_etd)



Part of the [Mechanical Engineering Commons](#), [Mechanics of Materials Commons](#), and the [Oil, Gas, and Energy Commons](#)

---

### Recommended Citation

Alexander, David, "Suitability of Low-Cost Additive Manufacturing for Polymer Electrolyte Fuel Cells" (2022). *Open Access Theses & Dissertations*. 3469.  
[https://scholarworks.utep.edu/open\\_etd/3469](https://scholarworks.utep.edu/open_etd/3469)

This is brought to you for free and open access by ScholarWorks@UTEP. It has been accepted for inclusion in Open Access Theses & Dissertations by an authorized administrator of ScholarWorks@UTEP. For more information, please contact [lweber@utep.edu](mailto:lweber@utep.edu).

SUITABILITY OF LOW-COST ADDITIVE MANUFACTURING FOR POLYMER  
ELECTROLYTE FUEL CELLS

DAVID ALEXANDER IV

Doctoral Program in Aerospace and Mechanical Engineering

APPROVED:

---

Calvin Stewart, Ph.D., Chair

---

Yirong Lin, Ph.D.

---

Eric MacDonald, Ph.D.

---

Rodney Borup, Ph.D.

---

Tommy Rockward, M.S.

---

Stephen Crites, Ph.D.  
Dean of the Graduate School

SUITABILITY OF LOW-COST ADDITIVE MANUFACTURING FOR POLYMER  
ELECTROLYTE FUEL CELLS

by

DAVID ALEXANDER IV, B.S., M.S.

DISSERTATION

Presented to the Faculty of the Graduate School of

The University of Texas at El Paso

in Partial Fulfillment

of the Requirements

for the Degree of

DOCTOR OF PHILOSOPHY

Department of Aerospace and Mechanical Engineering

THE UNIVERSITY OF TEXAS AT EL PASO

May 2022

## ACKNOWLEDGEMENTS

The journey to the doctorate has been an enriching and fulfilling experience. This process has produced personal and professional advancement in my life. I would like to acknowledge all the people that have poured into me during this process.

First, I would like to thank my advisor, Dr. Calvin Stewart, for his guidance and support from the moment I decided to attend the University of Texas at El Paso. He provided opportunity and significant insight to the world of academic research and professorship for me.

Second, I would like to thank my co-advisor and mentor, Tommy Rockward. His mentorship has been invaluable since I first arrived at Los Alamos National Laboratory. Tommy had a unique way of keeping me in the right situations to spark growth technically and personally. I will forever carry your wise words and approaches to life. I also would like to thank the National Nuclear Security Administration sponsored African American Partnership Program and Minority Serving Institution Partnership Program (Julie Spyres, Jenny Kline, and David Canty) for the financial support and career path guidance.

Next, I would like to thank Simone Buford, Dr. André Spears, Jacob Pellicotte, and Elliot Dean for always providing listening ears and unique insight to obstacles I found myself faced with throughout my journey. The different perspectives internal and external of STEM greatly helped me to produce well rounded solutions to impact a wider range of stakeholders. Special thanks to Dr. Rodney Borup, Dr. Eric MacDonald, and Dr. Yirong Lin for taking the time to serve on my dissertation committee and contributing your expert feedback. Additional thanks to Dr. Lin for all the opportunities, resources, and encouraging words you provided as the Graduate Program Director at the University of Texas at El Paso. I would also like to thank the Lovato family/friends

and the Pellicotte family/friends for providing a “home away from home” as I traveled back and forth between Los Alamos and El Paso your lovingkindness shall never be forgotten.

Last and most importantly, I would like to thank my family for the unconditional love and support. Their belief in me inspires me to continually press forward despite the challenges. Special thanks to my grandfather, David Alexander Jr. for telling me as a little boy that I would have, “Dr” in front of my name someday and to always play on my harp. Granddaddy, that day is here!

## ABSTRACT

The purpose of this dissertation is to study the feasibility of low-cost additive manufacturing to fabricate polymer electrolyte fuel cell bipolar plate materials. Traditional manufacturing techniques include molding, milling, hollow embossing, hydro-forming, rolling, and electromagnetic forming. These processes are employed when a design has been selected due to higher costs at low volumes. The combination of high initial costs and bipolar plates being the most expensive component of the polymer electrolyte fuel cell creates incentive to mitigate this obstacle.

The feasibility of low-cost additive manufactured bipolar plates will be proven by fabrication, post-processing, and characterization of printed test specimen. The material selected for this study is Titanium Grade 2. The additive manufacturing method, bound metal deposition, via material extrusion is the process employed to create various test designs with ease. Post-processing is completed using a hot isostatic press and thermal sintering approach to be compared. In-situ and ex-situ experimental test are conducted to obtain electrical, and electrochemical properties of titanium grade 2 as a bipolar plate material.

The significance of this study is the reduction of bipolar plate design costs experienced in the development stages prior to mass production and unveil new approaches to creating bipolar plate systems with composite materials. Rapid manufacturing is the implementable approach to exploit this cost related issue because of its low cost at low volumes relationship to production. Considering the evolution of bipolar plate designs over the years, the success of this study is an asset to the iterative nature of optimizing bipolar plate designs, materials, and systems for polymer electrolyte fuel cells.

TABLE OF CONTENTS

ACKNOWLEDGEMENTS..... III

ABSTRACT..... V

LIST OF TABLES..... IX

LIST OF ABBREVIATIONS.....XIII

CHAPTER 1. CHAPTER 1: INTRODUCTION..... 1

    1.1 MOTIVATION ..... 1

    1.2 LITERATURE REVIEW ..... 3

    1.3 RESEARCH OBJECTIVES..... 18

    1.4 ORGANIZATION ..... 18

CHAPTER 2. MATERIAL AND EQUIPMENT..... 20

    2.1 INTRODUCTION..... 20

    2.2 BOUND METAL DEPOSITION..... 20

    2.3 TITANIUM-POLYLACTIC ACID COMPOSITE..... 21

    2.4 SINTERING..... 26

    2.5 CORROSION TESTING ..... 29

    2.6 HARDNESS TESTING ..... 31

    2.7 SUMMARY ..... 32

CHAPTER 3. MATERIAL CHARACTERIZATION ..... 33

    3.1 INTRODUCTION..... 33

    3.2 SCANNING ELECTRON MICROSCOPY-ENERGY DISPERSIVE X-RAY SPECTROSCOPY

3.3	X-RAY FLUORESCENCE .....	36
3.4	X-RAY COMPUTED TOMOGRAPHY .....	37
3.5	OPTICAL PROFIOMETRY .....	39
3.6	THERMOGRAVIMETRIC ANALYSIS- MASS SPECTROSCOPY .....	43
3.7	SUMMARY .....	43
CHAPTER 4. SINTERING OPTIMIZATION .....		45
4.1	SEM CHARACTERIZATION .....	45
CHAPTER 5. POST PROCESSING OF PRINTED TEST SPECIMEN.....		50
5.1	HOT ISOSTATIC PRESSING .....	50
5.2	THERMAL SINTERING .....	53
5.3	SUMMARY .....	54
CHAPTER 6. BIPOLAR PLATE CHARACTERIZATION .....		56
6.1	OPTICAL PROFIOMETRY .....	57
6.2	ENERGY DISPERSIVE X-RAY SPECTROSCOPY .....	59
6.3	ELECTRICAL PROPERTIES .....	61
6.4	CORROSION RESISTANCE .....	62
6.5	HARDNESS TESTING .....	66
6.6	SUMMARIZE .....	66
CHAPTER 7. CONCLUSIONS/FUTURE WORKS .....		68
7.1	CONCLUSIONS .....	68
7.2	FUTURE WORK.....	68
7.3	ALTERNATIVE TOPICS .....	69

REFERENCES .....	70
VITA.....	75

LIST OF TABLES

Table 1. Metal AM processes and cost associated..... 9

Table 2. Chemical composition of Titanium Grade 2 [51]. ..... 22

Table 3. 2030 DOE targets for BPP [54]. ..... 57

Table 4. Electrical Properties of AM specimen vs. baseline BPP ..... 61

Table 5. Current densities of test specimen from corrosion testing..... 66

Table 6. Rockwell Hardness B of test specimen before and after thermal sintered in argon. .... 66

## LIST OF FIGURES

Figure 1. Electrochemical process of PEMFC [1] .....	1
Figure 2. Schematic view of PEFC cross section [2].....	2
Figure 3. Graphite bipolar plate [7]. .....	4
Figure 4. Polymer composite bipolar plate [15]. .....	5
Figure 5. Compression molding approach for bipolar plate production [16]. .....	6
Figure 6. Compression molding approach for bipolar plate production [16]. .....	6
Figure 7. Metallic bipolar plate [17]. .....	7
Figure 8. Physical vapor deposition process [22]. .....	8
Figure 9. Cross-sectional view of a coated bipolar plate .....	9
Figure 10. Schematic of EBM components [36]. .....	10
Figure 11. Schematic of SLM components [37].....	11
Figure 12. Schematic of DED systems (laser and electron beam) [38]. .....	12
Figure 13. Schematic of BJ process [39]. .....	13
Figure 14. Schematic of the material extrusion process [40].....	14
Figure 15. Image of common necking feature to monitor sintering [41].....	15
Figure 16. Illustration of porosity due to agglomeration [45]. .....	17
Figure 17. BMD process for candidate material. ....	20
Figure 18. Optical microscopy of titanium PLA composite. ....	21
Figure 19. Titanium grade 2 composite filament [51]. .....	23
Figure 20. CreatBot F430 material extrusion 3D printer. ....	24
Figure 21. 3D printed parts for testing using optimized settings. ....	25
Figure 22. TGA-MS setup at LANL.....	26

Figure 23. 1500°C MTI Muffle Furnace at UTEP.....	27
Figure 24. HIP setup at American Isostatic Presses [52].....	28
Figure 25. Proteus Alpha Electrochemical Cell at LANL.....	29
Figure 26. Tafel plot for corrosion [53].....	30
Figure 27. Buehler Hardness Tester at LANL.....	31
Figure 28. Optical Microscopy of Ti-grade 2 printed part (a) close-up of filament with 1.75 mm diameter (b) micrograph of visible Ti-grade 2 powder in the PLA matrix.....	33
Figure 29. SEM and EDS of composite filament surface.....	34
Figure 30. SEM and EDS of the sintered composite filament surface.....	35
Figure 31. XRF mapping of printed material (a) before and (b) post debinding and sintering....	36
Figure 32. Full tomography and 50% of composite filament cross-section via XCT.....	37
Figure 33. Full tomography and 50% of composite filament post sintering.....	38
Figure 34. 3D roughness profile of as-received composite filament.....	39
Figure 35. Profilometry of as-received composite filament with roughness values.....	40
Figure 36. Profilometry of post sintered composite filament with roughness values.....	41
Figure 37. 3D roughness profile of sintered composite filament.....	42
Figure 38. TGA-MS of the composite filament at 1400°C.....	43
Figure 39. Sintering at 1350°C as recommended by the Virtual Foundry.....	45
Figure 40. Over-sintering of the titanium filament at 1450°C.....	46
Figure 41 Sintering of the titanium filament at 1400°C.....	47
Figure 42. Sintering of printed cube at 1400°C.....	48
Figure 43. Sintering of printed disc at 1400°C.....	49
Figure 44. HIP of test specimen at 1400°C in air.....	50

Figure 45. HIP of the test specimen at 1400°C in argon. ....	51
Figure 46. Machined HIP sintered cube at 1400°C. ....	52
Figure 47. Thermal sintering of printed plate at 1400°C in air.....	53
Figure 48. Sintering of printed plate at 1400°C in nitrogen. ....	54
Figure 49. Baseline BPP used in PEFC stack at LANL. ....	56
Figure 50. Optical microscopy of the (a) HIP cube vs. the (b) baseline BPP.....	57
Figure 51. Topography of the (a) HIP cube vs. the (b) baseline BPP.....	58
Figure 52. Topography of (a) thermal sintered Ar and (b) baseline BPP. ....	58
Figure 53. EDS mapping of the HIP cube. ....	59
Figure 54. EDS mapping of thermal sintered in Argon specimen.....	60
Figure 55. EDS mapping of the thermal sintered N <sub>2</sub> specimen. ....	61
Figure 56. Tafel plot of the baseline BPP vs Ag/AgCl reference.....	62
Figure 57. Tafel plot of the HIP cube vs Ag/AgCl reference. ....	63
Figure 58. Tafel plot of the specimen thermal sintered in N <sub>2</sub> vs Ag/AgCl reference.....	64
Figure 59. Tafel plot of the thermal sintered Ar specimen vs Ag/AgCl reference.....	65

## LIST OF ABBREVIATIONS

SYMBOL	DESCRIPTION
DOE	Department of Energy
PEFC	Polymer Electrolyte Fuel Cell
BPP	Bipolar Plate
MEA	Membrane Electrode Assembly
AM	Additive Manufacturing
BMD	Bound Metal Deposition
DED	Directed Energy Deposition
EBM	Electron Beam Melting
SLM	Selective Laser Melting
BJ	Binder Jetting
MJ	Material Jetting
MIM	Metal Injection Molding
Ti-2	Titanium Grade 2
PLA	Poly-lactic Acid
TGA	Thermo-Gravimetric Analysis
MS	Mass Spectroscopy
OP	Optical Profilometry
SEM	Scanning Electron Microscopy
3D	Three Dimensional
EDS	Energy Dispersive Spectroscopy
XRF	X-ray Fluorescence

XCT	X-ray Computed Tomography
OM	Optical Microscopy

# CHAPTER 1. CHAPTER 1: INTRODUCTION

## 1.1 Motivation

Polymer electrolyte fuel cells (PEFC) have an overall efficiency up to 60% compared to 33-35% for conventional combustion-based power plant and less than 20% for gasoline engines with virtually no carbon emissions. PEFCs can operate at low temperature, start quickly, have a high-power density and energy conversion efficiency; and are easily scaled [1]. Applications for this system ranges from transportation technologies including personal, industrial, and commercial vehicles to stationary distributed power generation for facilities to portable devices that typically uses batteries.

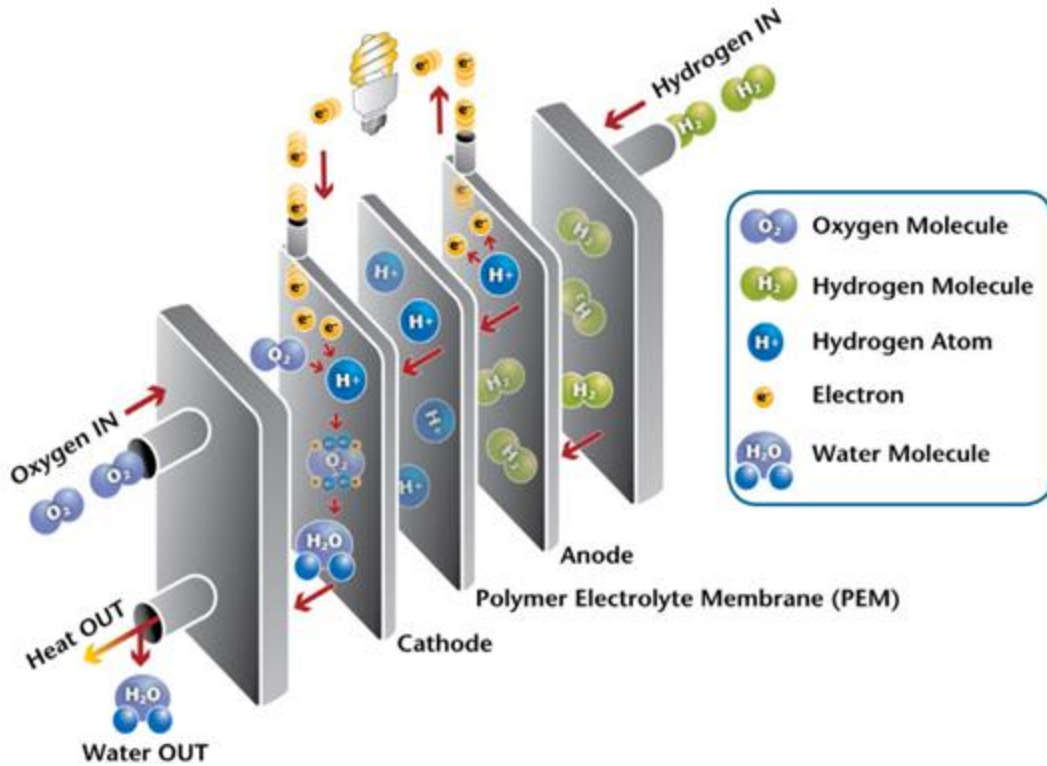


Figure 1. Electrochemical process of PEMFC [1]

The working principle of the PEFC is the conversion of chemical energy in hydrogen to electricity, with the only by-products being water and heat; an electrochemical process is illustrated in Figure 1. The components that make up an individual cell in the system is a polymer

electrolyte, two electrodes (anode and cathode), gaskets, and bipolar plates (BPP). Furthermore, the individual cell can be placed in series to create a fuel cell stack. When the PEFC is stacked in series, the power output is the summation of all connected cells. The BPP and gasket components are referred to as the PEFC hardware, where the responsibilities are fluid distribution and management (reactant gas and water), current collection, and gas containment within the system.

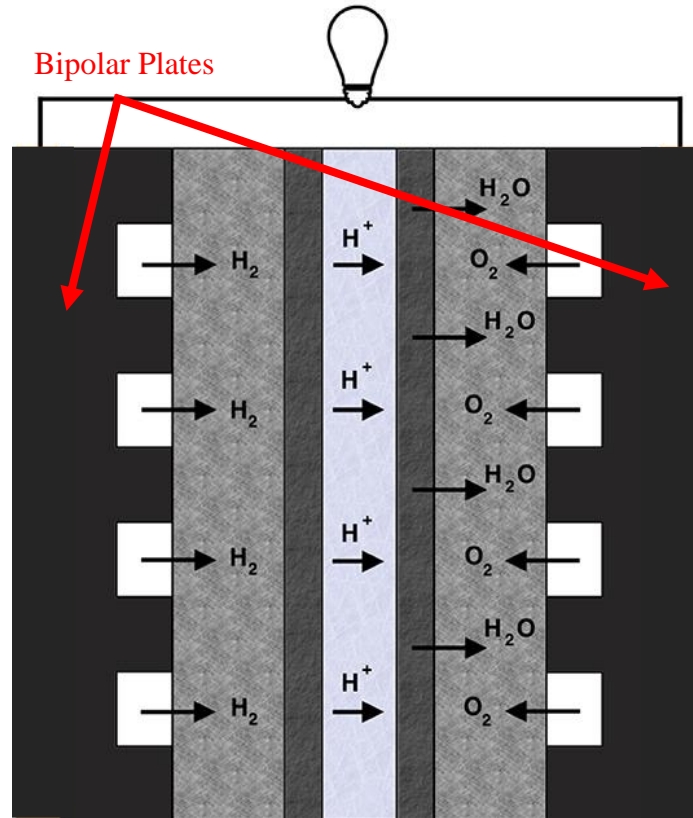


Figure 2. Schematic view of PEFC cross section [2]

For the gas sealability, the BPP serves as the structural interface for the gasket to contain the reactant gases but allow the excess water to be wicked to the periphery for evaporation. Cross section of PEFC is shown in Figure 2 [2]. Despite much progress since the inception of the fuel cell in 1839, cost reduction and improving durability are persisting limitations to the ubiquitous commercialization of the fuel cell [3]. Ongoing research is centered around material development of the components, including hardware, to reduce costs and extend the lifetime of the fuel cell.

Additive manufacturing (AM) can be a powerful tool for refining a design to optimize performance. Furthermore, with the printability of engineering materials, AM can also be economic for low-volume end-use parts. While low-cost, high volume manufacturing processes will aid in making the fuel cell cost-competitive with conventional technologies, AM can be employed to rapidly iterate designs complementing the new materials to reduce costs and improve durability [4-**Error! Reference source not found.**]. Traditional manufacturing and AM have specified points in the production process where they can add value to a product. Conventional technologies are most advantageous when the designs are already configured and ready for high volume production. Additive technologies are best in the design phase when features are still being optimized for maximum performance and the volume is low. The focus of this study is to evaluate a low-cost additive manufacturing technology for its feasibility as a rapid prototyping technique for PEFC bipolar plates.

## 1.2 Literature Review

The BPP is an important component in the PEFC functionally and financially. It has vital roles including electron conduction, fluid management, and heat dissipation. Crucial factors that determine BPP viability are electrical conductivity, corrosion resistance, thermal conductivity, gas permeability, mechanical strength, formability, and cost-weight. This key PEFC component accounts for approximately 80% of the total weight and 45% of the total cost of the entire system [4]. The BPP possesses a dominant structural influence on the dimensions, performance, and lifetime of the PEFC. Dimensions vary based on the manufacturing process i.e., machined or formed in addition to the material selected. Graphite materials tend to be bulkier due to

manufacturing complications while metallic materials can be thin because of its machinability. Flowfield geometries and fluid management techniques of electrochemical constituents and byproducts strongly influence performance. Standing water in addition to thermal conditions can induce material delamination and cracking [6]. The corrosion resistance of the material dictates how long a BPP can operate in service and perform as expected. As the metal corrodes, ions leach into the polymer membrane causing peroxide formation. The evolution of the peroxide then leads to the decomposition of the membrane producing sulfuric acid and fluorine compounds including hydrogen fluoride [8].



Figure 3. Graphite bipolar plate [7].

The BPP component can be comprised of different material categories, e.g., graphite, polymer composites, and metal. These materials can also be combined to make composite systems or used to impregnate a matrix as additives. The material selection plays a major role in the broader perspective of performance strategy, manufacturing, and mass production. Graphite bipolar plates possess material advantages including high electron conductivity, good corrosion resistance and low density.



Figure 4. Polymer composite bipolar plate [15].

Contrarily, graphite has low machinability due to its brittle nature in addition to low electrical and thermal conductivity relative to metals. Furthermore, graphite is porous which rules out the possibility of reducing the weight, volume, and internal resistances by decreasing the thickness. A graphite plate is shown in Figure 3 Polymer composite BPPs can be manufactured employing traditional processing approaches including compression molding and injection

molding [9-14]. The methods provide a significant time-cost savings compared to engraving or milling the flow channels. The polymer composite bipolar plate is shown in Figure 4.

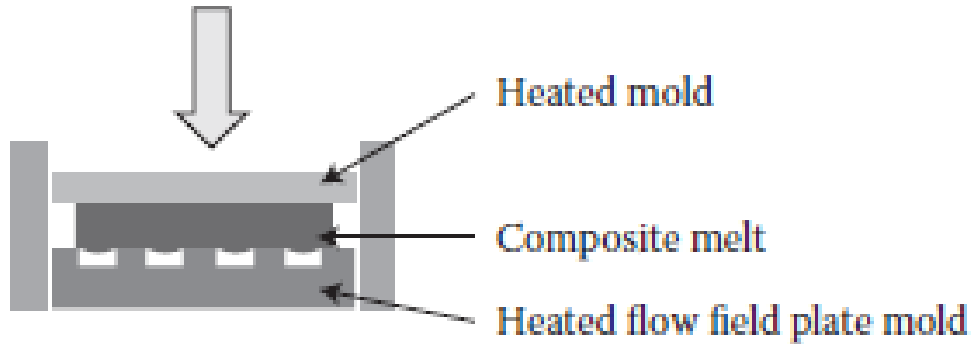


Figure 5. Compression molding approach for bipolar plate production [16].

The processing time and cost for compression molding is higher than injection molding. Regardless of the apparent advantages, the plate dimensionality is a challenge to control due to the warping and thermal deformation. Also, there is a great compromise between mechanical strength and electron conductivity regarding the impregnation of additives. The more the matrix is saturated in hopes of achieving proper electrical conductivity, the more brittle the plate becomes. The compression molding process for BPPs is illustrated in Figure 5.

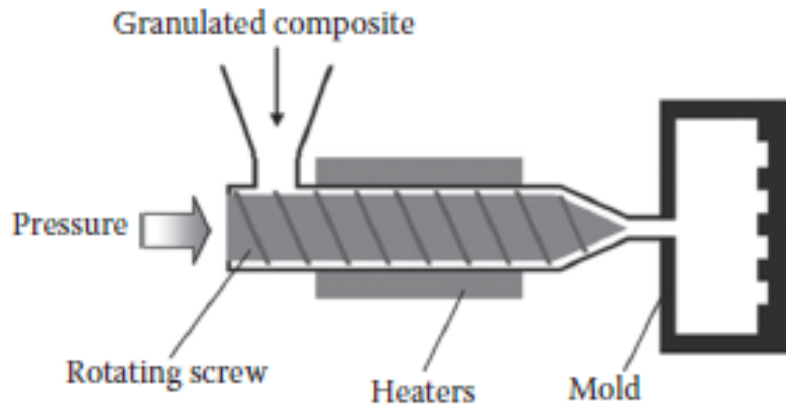


Figure 6. Compression molding approach for bipolar plate production [16].

The injection molding production process is shown in Figure 6. Metallic bipolar plates reduce weight costs without sacrificing important properties like electrical and thermal conductivity, mechanical properties, machinability, and gas sealability. This is achievable due to reduced thicknesses compared to bulkier graphite BPPs. A metallic bipolar plate is shown in Figure 7. Thin metal sheets as base material can range between 0.1 to 0.5 mm. When it comes to cost-efficient production, that thickness range offers a variety of advantages due to processes like stamping and high-pressure metal forming [17].

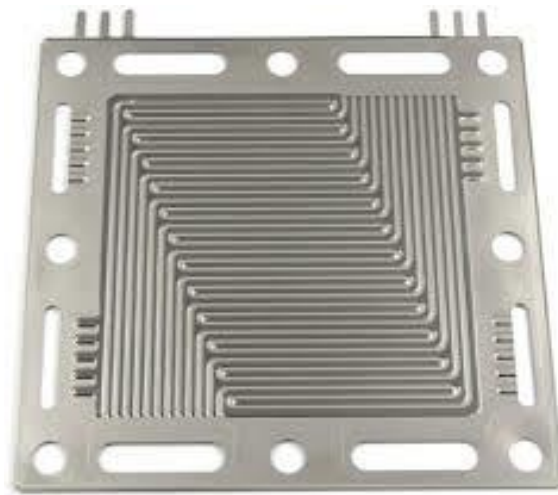


Figure 7. Metallic bipolar plate [17].

However, uncoated bipolar plates are susceptible to corrosion in the PEFC environment due to crucial electrochemical potentials. This causes the material to enter trans passive regions where rapid dissolution ensues [18]. Thus, leaching metal ions poison the membrane reducing the power density due to degradation [19]. Vital characteristics for the metal BPP evaluation is the understanding of corrosion mechanisms and the balance of passivation layers with electron conductivity preservation. For metallic bipolar plates to be effective, the exposed surface must be treated with a protective passivation layer to decrease the affection of the corrosive environment.

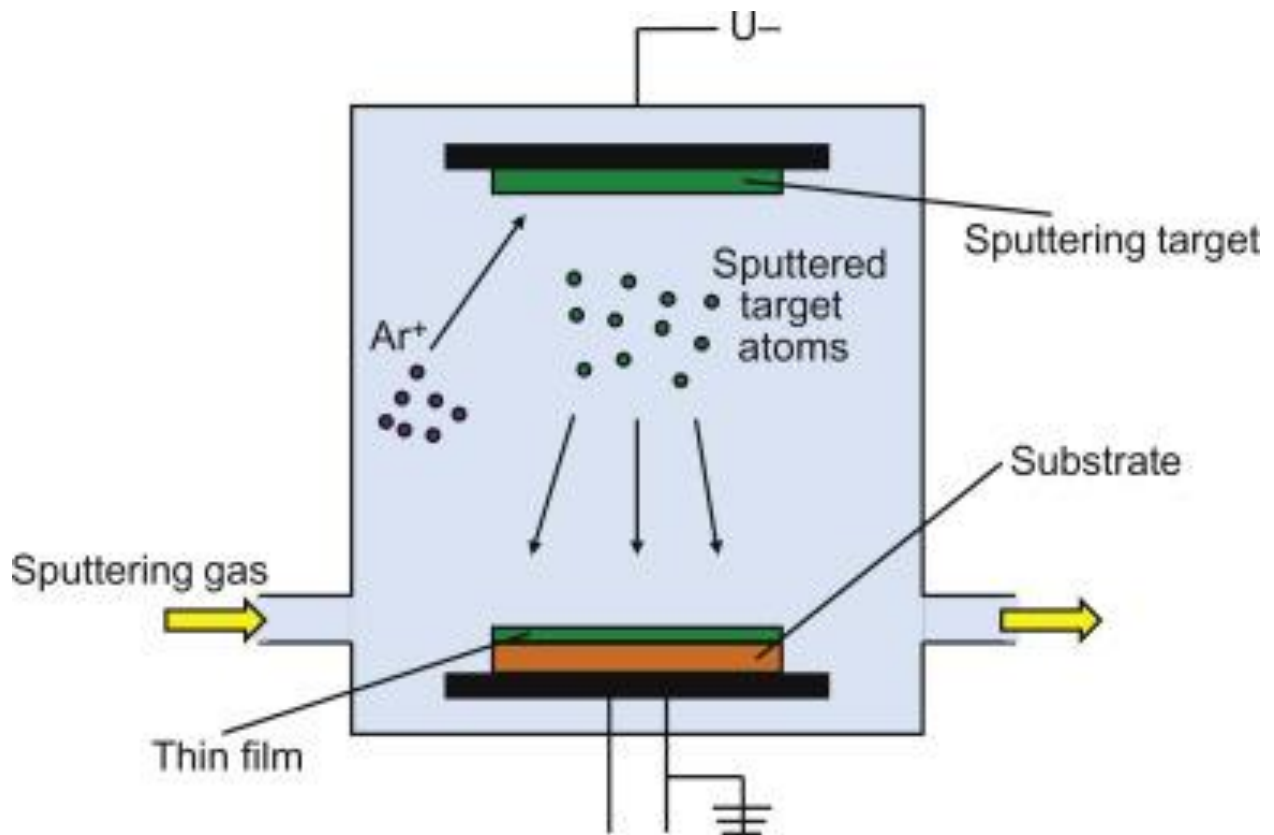


Figure 8. Physical vapor deposition process [22].

Functional coatings and surface modifications are employed to protect the base metal substrate when used as a BPP. Coatings were initially perceived to possess homogenous defect-free layers; however, it has been shown that graded layering can outperform the uniform coats [20-21].

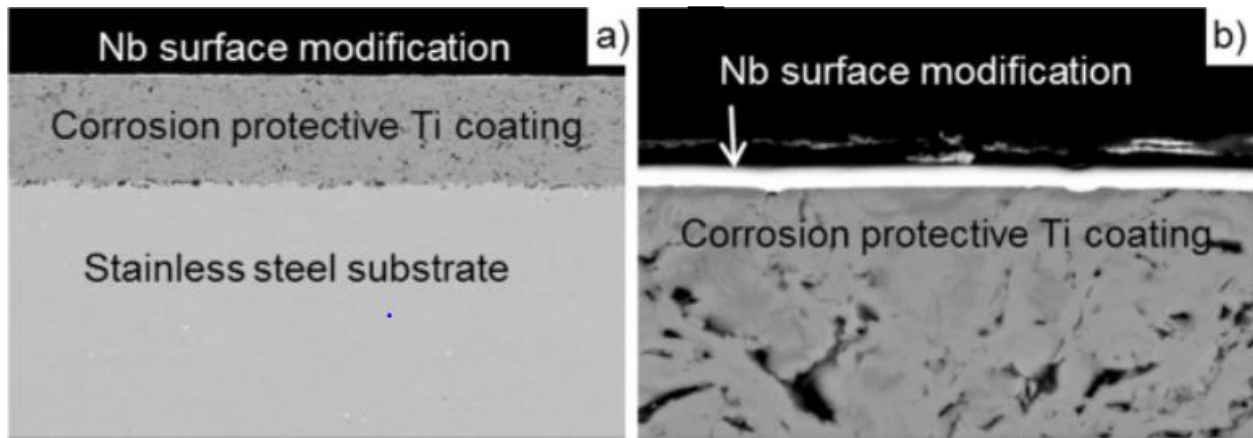


Figure 9. Cross-sectional view of a coated bipolar plate

Surface modification techniques include electrodeposition, physical vapor deposition, sputtering, and high energy micro-arc alloying. An illustration of the common coating process physical vapor deposition is shown in Figure 8. Titanium is a material that is commonly used as a base material and surface modification compound to improve BPP performance in the PEFC through corrosion resistance and electrical conductivity [23-32]. A coated bipolar plate cross-section is shown in Figure 9.

Table 1. Metal AM processes and cost associated.

AM Process	Cost	Reference
Electron Beam Melting	\$100k - \$250k	[56]
Binder Jetting	\$150k - \$225k	[57]
Selective Laser Melting	\$170k - \$300k	[58]
Direct Energy Deposition	\$700k - \$1.2 million	[59]

Additive manufacturing (AM) has proved its worth regarding the ability to change how energy systems are designed and employed. The ability to manufacture complex 3D structures, with bespoke design freedoms including mass customization, topology optimization, and surface texturing offers drastic potential for fuel cell design innovation [34]. The methods used for metal AM include electron beam melting (EBM), selective laser melting (SLM), binder jetting (BJ),

direct energy deposition (DED), and bound metal deposition (BMD). Metal AM systems range in price, reaching as high as a few million dollars. Costly components such as electron beams, vacuums, and lasers increase the price for the EBM, SLM, BJ and DMLS manufacturing methods. Also, these processes incur indirect costs for facilities to accommodate the demand of the machines. The expensive metal printing systems operate best when ambient temperature and humidity are consistent with manufacturer recommendations.

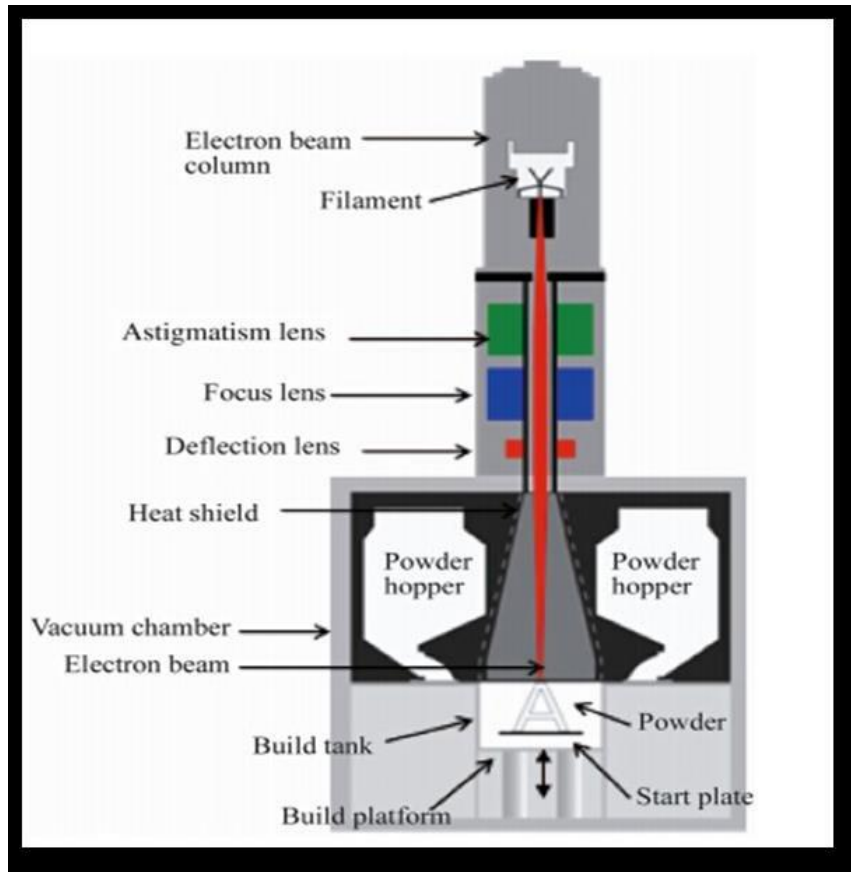


Figure 10. Schematic of EBM components [36].

The EBM process is performed by selectively melting powders using an electron beam. The electron beam is a power source that must be enabled under vacuum conditions to prevent dissipation of the electrons leveraged to melt the feedstock powder. The electrons are emitted via tungsten filament where they are accelerated to almost half of lightspeed and controlled by

magnetic fields. These magnetic fields focus and deflect the beam to determined spatial locations [35-36]. The EBM equipment is shown in Figure 10

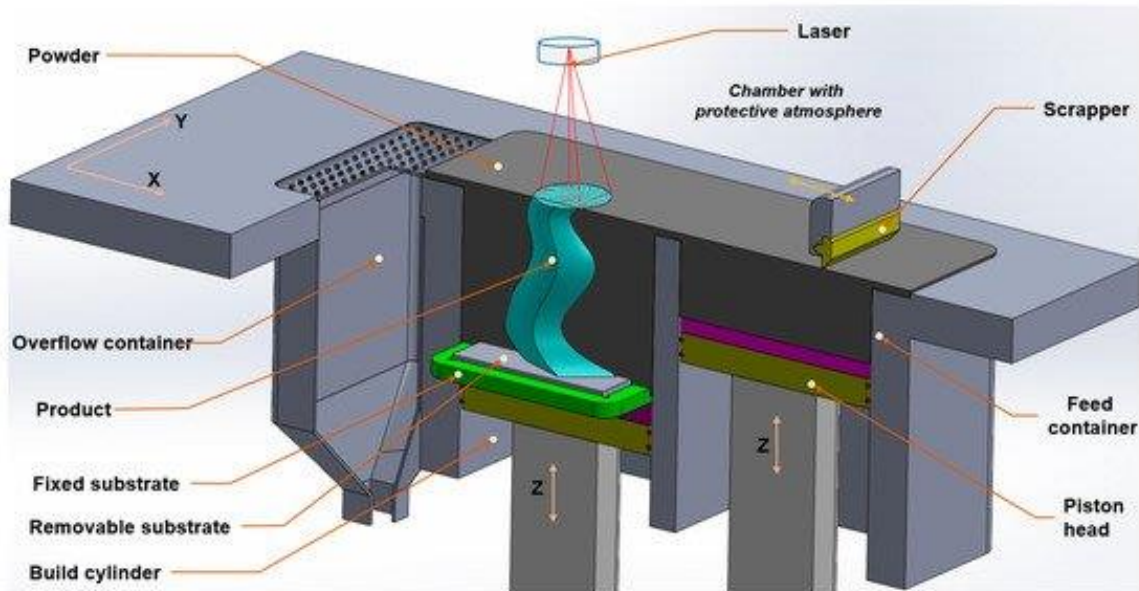


Figure 11. Schematic of SLM components [37].

A similar yet different process, SLM is one of the industry's leading AM technologies. This process uses a laser source to selectively melt powder particles to form the final part. Like EBM, a thin layer of powder is spread across the build plate. Then the laser selectively scans the cross section on the material in the x-y axes and repeats that sequence while adding layers in the z-direction [35]. The SLM equipment is shown in Figure 11.

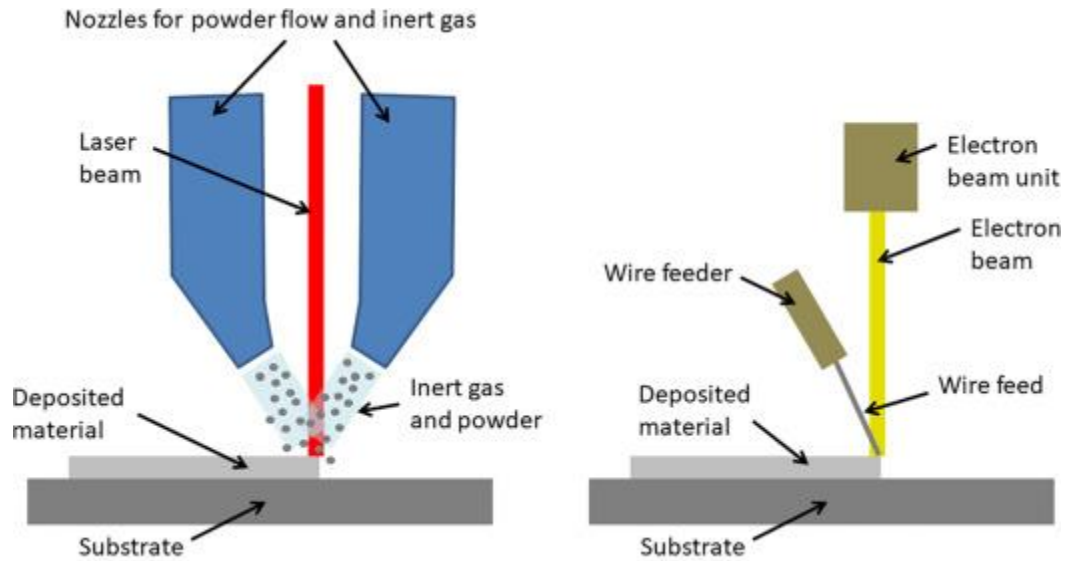


Figure 12. Schematic of DED systems (laser and electron beam) [38].

The DED process uses an energy source to simultaneously deposit and melt a feedstock material. The energy input can either be a laser, electron beam, or plasma arc. The feedstock can be a metal wire or powder. When the electron beam source is used, a vacuum is still required just like the EBM process. Alternatively, when the laser source is being used, inert gas is introduced with the powder. This is done to reduce the oxidation issues by protecting the melted region as it is being printed [35]. The DED equipment is shown in Figure 12.

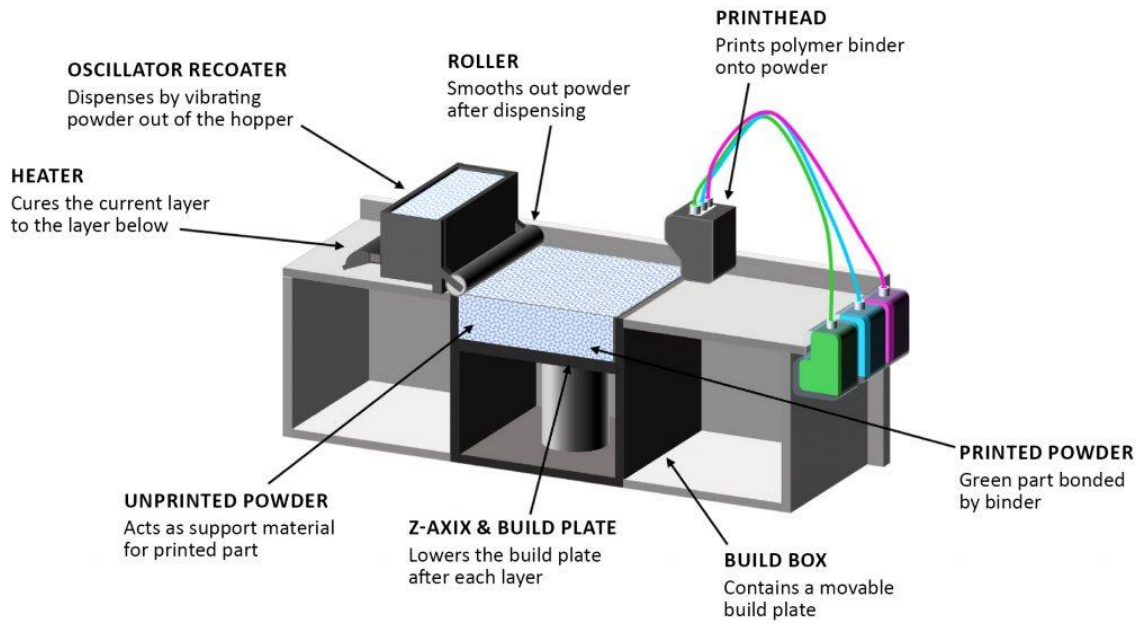


Figure 13. Schematic of BJ process [39].

The BJ process selective deposits a polymeric binder into a powder bed to fuse powder particles. The build plate is lowered in succession of each build layer to progressively build a part that require post-processing. In this process, majority of the powder feed is recycled. BJ requires a partial or full sintering to remove the binder and fuse the metal particles. This aspect of the process produces a finished component with the required properties [35]. The BJ equipment is shown in Figure 13.

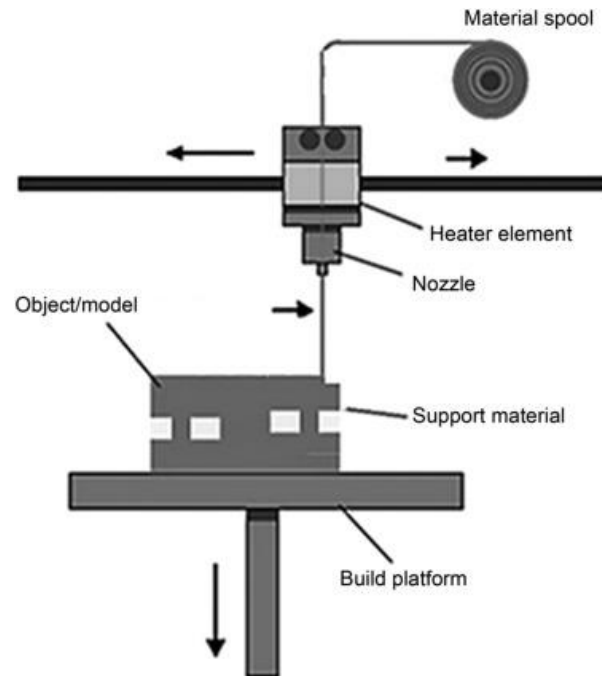


Figure 14. Schematic of the material extrusion process [40].

Material extrusion is an AM process where material is selectively dispensed through a heated nozzle. The material is heated to below the melting point to a soften state with flowability. The heated material is deposited layer-wise on a build platform according to the uploaded g-code. The nozzle translates in the x-y direction while the build stage moves vertically in the z-direction [35]. The material extrusion equipment is shown in Figure 14.

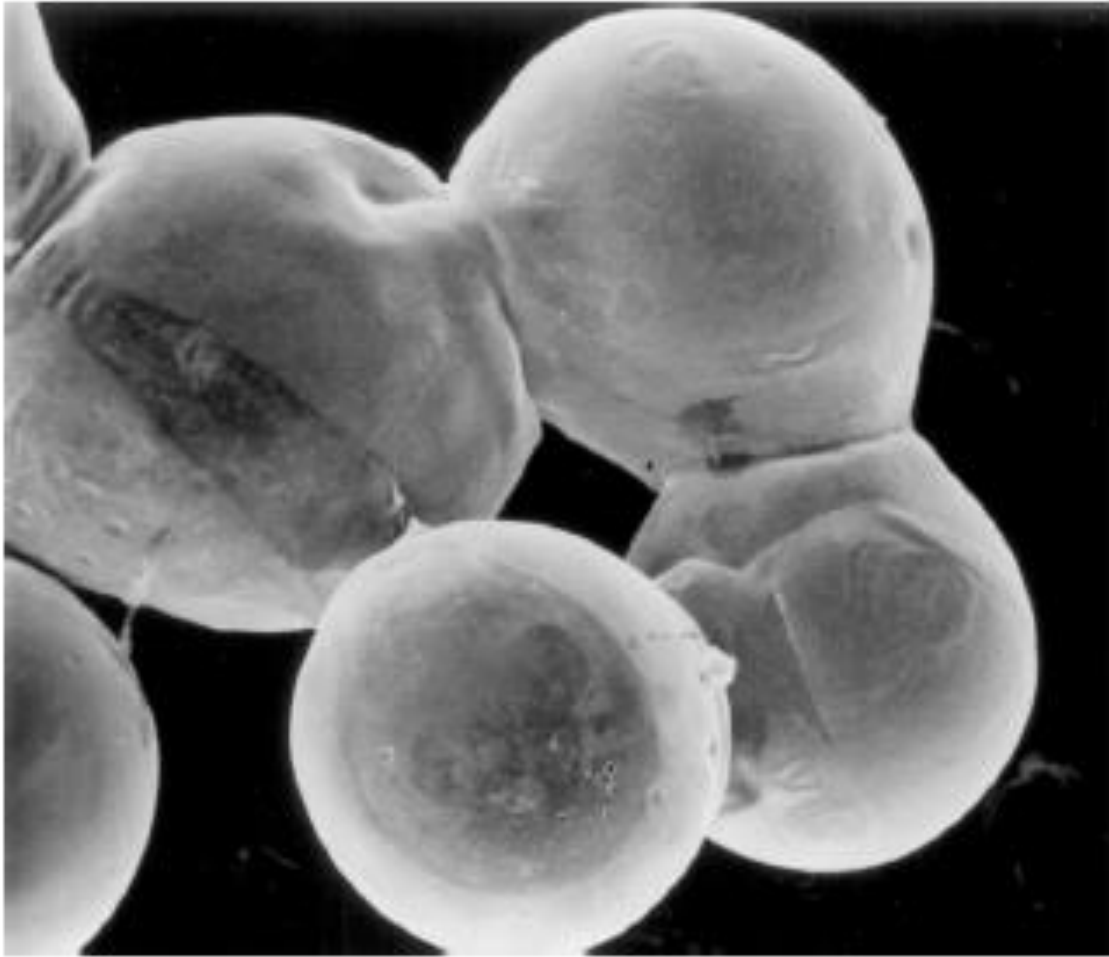
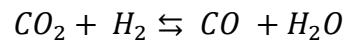


Figure 15. Image of common necking feature to monitor sintering [41].

Post processing is defined as any tasks that needs to be performed on a printed part for enhancement. Thermal post-processing can be used to alleviate residual stresses, reduce cracking, and homogenize the microstructure. Thermal processing techniques include hot isostatic pressing (HIP) and sintering. Thermal sintering or solid-state sintering is the process of fusing particles together below the melting point. Neck features between neighboring particles are the tell-tale sign of sinter progression and this observation is accomplished using scanning electron micrographs [41]. An image of sinter necking is depicted in Figure 15. Sintering is predicated on the temperature and soak time parameters. Titanium is typically sintered between the temperatures 1250 °C to 1400 °C and between the times of 120 to 240 minutes [42]. Successful sintering includes additional

factors such as furnace design, heating ramps, atmosphere as well as peak temperature and hold time. It is important to note that titanium can be over-sintered, so thermal protocols are customized to the powder and the furnace. The sintering atmosphere is the area encompassing the material. Various atmospheric conditions can yield different sintering reactions in the material. Nitrogen is an inert gas that can form nitrides at high temperatures and does not reduce the material. Argon is also inert and causes neither oxidation nor reduction. It also has low thermal conductivity. Air is an oxidized atmosphere with low thermal conductivity, slightly above argon [43]. Oxidation can be detrimental to metallic components, so the atmospheric control becomes significant. Inert gases like nitrogen and argon do not react with the lingering oxygen atoms, however carbon monoxide and hydrogen can react with oxides to form carbon dioxide or water vapor [44]. The atmospheric controlling reaction of components, carbon, hydrogen, and oxygen:



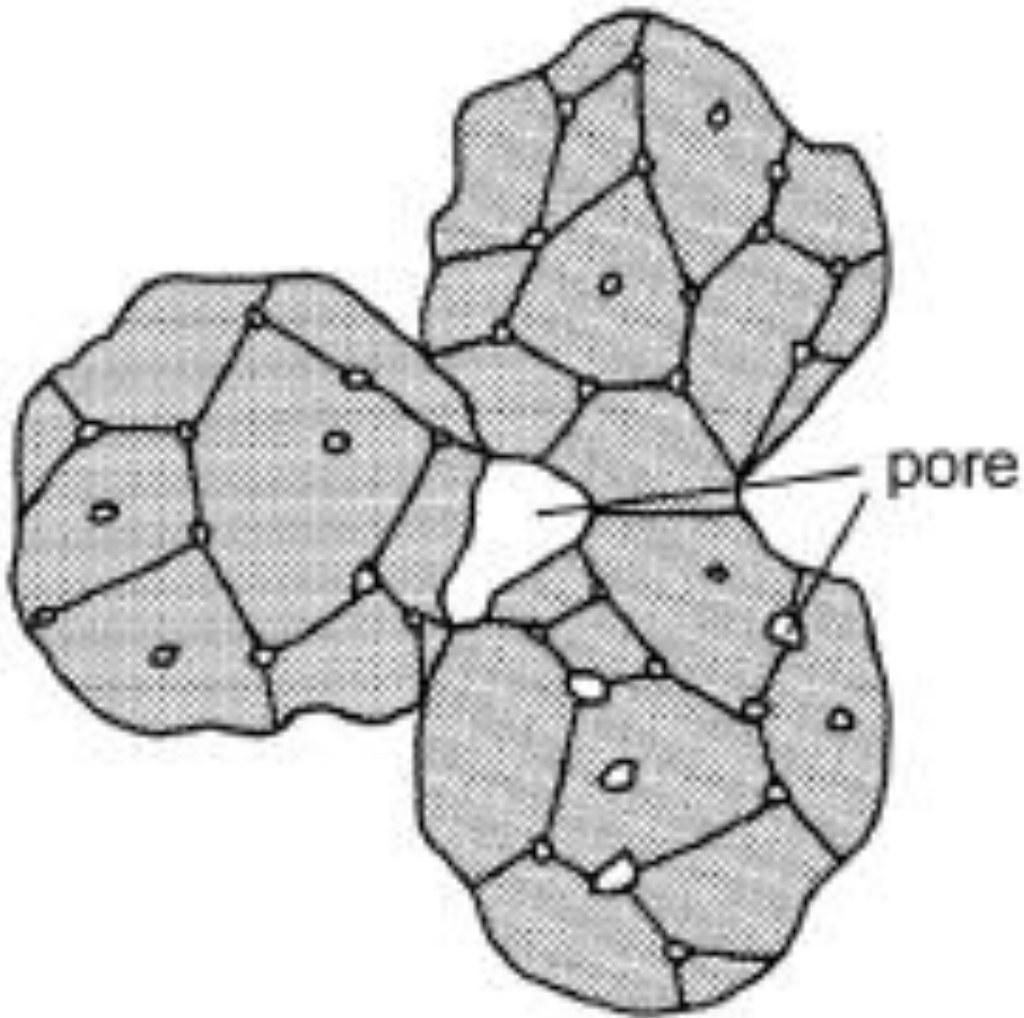


Figure 16. Illustration of porosity due to agglomeration [45].

Varying powder sizes can present a degraded sintering response by producing agglomerations. This feature inhibits densification because the small pores inside the particle agglomerates sinter and densify prematurely in the thermal cycle while the larger vacancies between agglomerates with longer diffusion distances slow down sintering and densification [45]. Porosity due to agglomerations is shown in Figure 16.

### 1.3 Research Objectives

The objective of this study is to qualify the electrical and corrosion properties of the AM candidate material for PEFC conditions. This dissertation work is considered valid upon the completion of these three objectives.

#### RO1: Characterize Material Pre/Post De-Binding and Post Sintering

The goal of this objective is to verify the AM material, understand the de-binding conditions, and achieve proper sintering conditions. This will be confirmed by evaluating the micrographs from SEM/EDS to observe a smooth microstructure coupled with elemental analysis.

RO2: Produce Test Samples Appropriate for BPP Using Low-Cost AM method and post-processing.

The goal of this objective is to print and process test specimen appropriate for the BPP material characterization study.

#### RO3: Material Characterization of Samples to Identify Compatibility as BPP Materials

The goal of this objective is to characterize the electrical and corrosion properties of the sintered titanium in comparison to the 2030 DOE targets for electrical conductivity, area specific resistance, and corrosion resistance. Meeting the electrical requirements qualifies the sintered titanium to function as a conductor of the electrons generated from the electrochemical reaction inside the PEFC and sufficiently corrosion resistant to withstand the service conditions and lifetime.

### 1.4 Organization

The work in this dissertation is organized as follows. Chapter 2 introduces the material and equipment used in this study. Chapter 3 entails the material characterization of the titanium-PLA composite with corresponding remarks to confirm the filament and its quantities are as advertised. Chapter 4 contains the optimization of the sintering parameters of the titanium composite with the

respective data. Chapter 5 presents the processing of the test specimen with corresponding remarks of its appropriateness for BPP characterization. Chapter 6 presents the bipolar plate characterization which includes corrosion resistance properties, area specific resistance, electrical conductivity, and hardness values of the sintered titanium. Remarks comparing the acquired results to the DOE targets shall be included. Chapter 7 contains final remarks regarding the feasibility of low-cost AM for PEFC bipolar plates and ideas for future work.

## CHAPTER 2. MATERIAL AND EQUIPMENT

### 2.1 Introduction

In this chapter, the equipment and processes presented will introduce what material is used, how the low-cost AM method will fabricate test specimen, how the printed parts will be processed, and how the test specimen will be characterized in BPP conditions.

### 2.2 Bound Metal Deposition

An extrusion-based metal additive manufacturing process called BMD is used to construct the metal components [46-47]. The filament contains a binding additive and metal powders which is softened via resistance heater and extruded onto the build plate with three axes control. The binding additive serves as the media to print the metal powders into geometries of interest. Once the part is fabricated to its desired shape, the printed component must undergo debinding. This is where the binding additive is burned out at its thermal degradation temperature and the remaining metal powders begin to relocate in closer proximity of one another.

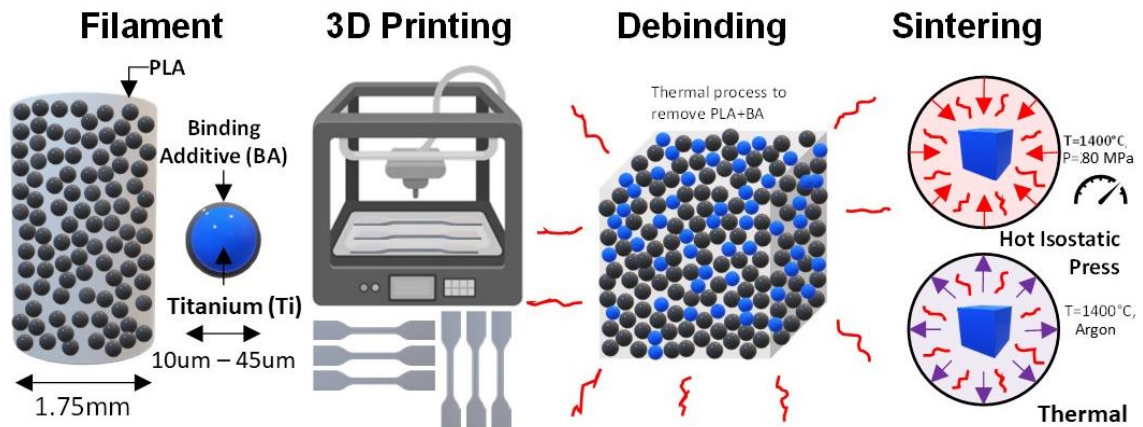


Figure 17. BMD process for candidate material.

Following the debinding stage is sintering, where the metal powders coalesce and densify. In this study, the parts will be sintered using heat for one set and a combination of heat and pressure

for another set to compare different sintering approaches. The BMD process from feedstock to thermal processing is illustrated in Figure 17.

The feedstock filament in this study is composed of titanium grade 2 powder bound in a PLA matrix to improve the encapsulation process and adhesion of particles. BMD is derived from metal injection molding (MIM), where metal powders are mixed into a polymer binder matrix to form the feedstock before injection into a die cavity. The material variety contain wide range of powder size distribution including fine powders.

### 2.3 Titanium-Polylactic Acid Composite

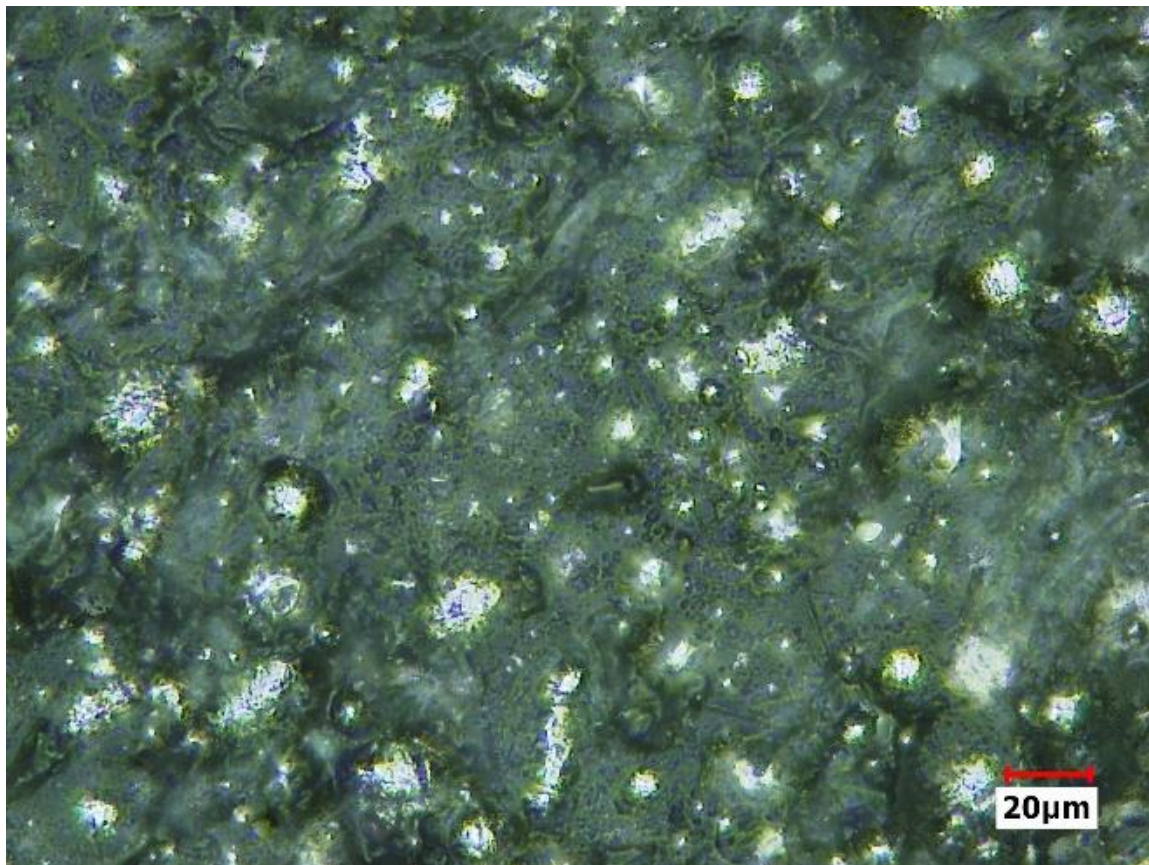


Figure 18. Optical microscopy of titanium PLA composite.

A composite material is a combination of two materials with different physical and chemical properties. When they are combined, they create a specialized material to accomplish a specific task. Titanium grade 2 powders are mixed into a polylactic acid (PLA) matrix then extruded and wound on a spool to create the metal-polymer composite feedstock. The PLA binder is a thermoplastic polyester with the backbone formula,  $(C_3H_4O_2)_n$ , widely used in additive manufacturing. An optical image of the composite material is shown in Figure 18.

Table 2. Chemical composition of Titanium Grade 2 [51].

Element	wt%
Carbon	0.01%
Iron	0.19%
Nitrogen	0.01%
Oxygen	0.25%
Hydrogen	0.002%
Titanium	Bal.

The material of interest is titanium grade 2, a pure alpha phase titanium, and is widely employed due to its moderate strength, excellent corrosion resistance, and formability. Typical applications for titanium grade 2 include, oil and gas components, reaction and pressure vessels, piping systems, heat exchangers, liners, and flue-gas desulphurization systems [48-50]. The chemical composition for the titanium grade 2 is found in Table 2.



Figure 19. Titanium grade 2 composite filament [51].

The composite feedstock used in this study is supplied by The Virtual Foundry as shown in Figure 19. The given metal content is 76.5% mass respectively. The metal powder distribution for the material used in this study is 10  $\mu\text{m}$  to 45  $\mu\text{m}$ . The density is 2.76 g/cc with as filament diameter of 1.75 mm. The recommended print parameters from The Virtual Foundry include nozzle temperature 210°C, print speed 66.66 mm/s, nozzle diameter 0.6 mm or higher, and flow volume 135%.

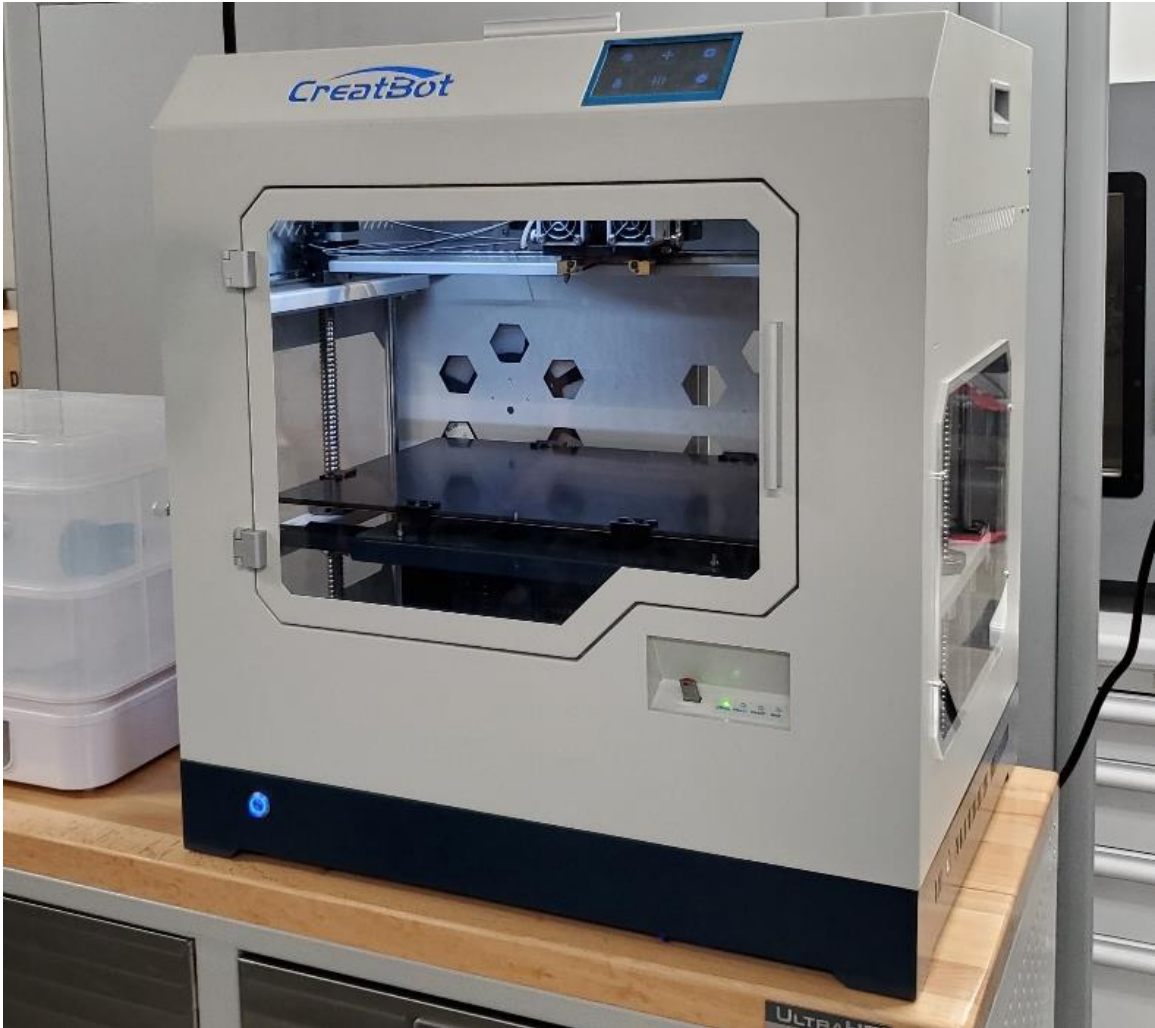


Figure 20. CreatBot F430 material extrusion 3D printer.

Sample fabrication was conducted in the Materials at Extremes Research Group (MERG) laboratory at The University of Texas at El Paso. The Creatbot F430 is a desktop material extrusion 3D printer that fabricated the samples in the study as shown in Figure 20. This 3D printer has a 400 mm x 300 mm x 300 mm build volume, resolution of 0.04 mm, dual extrusion nozzle with temperatures 260°C and 420°C, hot bed temperature 120°C, and hot chamber temperature 70°C. The optimized print parameters for the CreatBot F430 and CreatWare slicer include nozzle temperature 235°C, print speed 33.33 mm/s, nozzle diameter 0.6 mm, flow volume 100%.



Figure 21. 3D printed parts for testing using optimized settings.

Rectangular blocks in varying dimensions were fabricated to perform corrosion testing, electrical conductivity measurements, area specific resistance measurements. The printed parts are shown in Figure 21.

## 2.4 Sintering

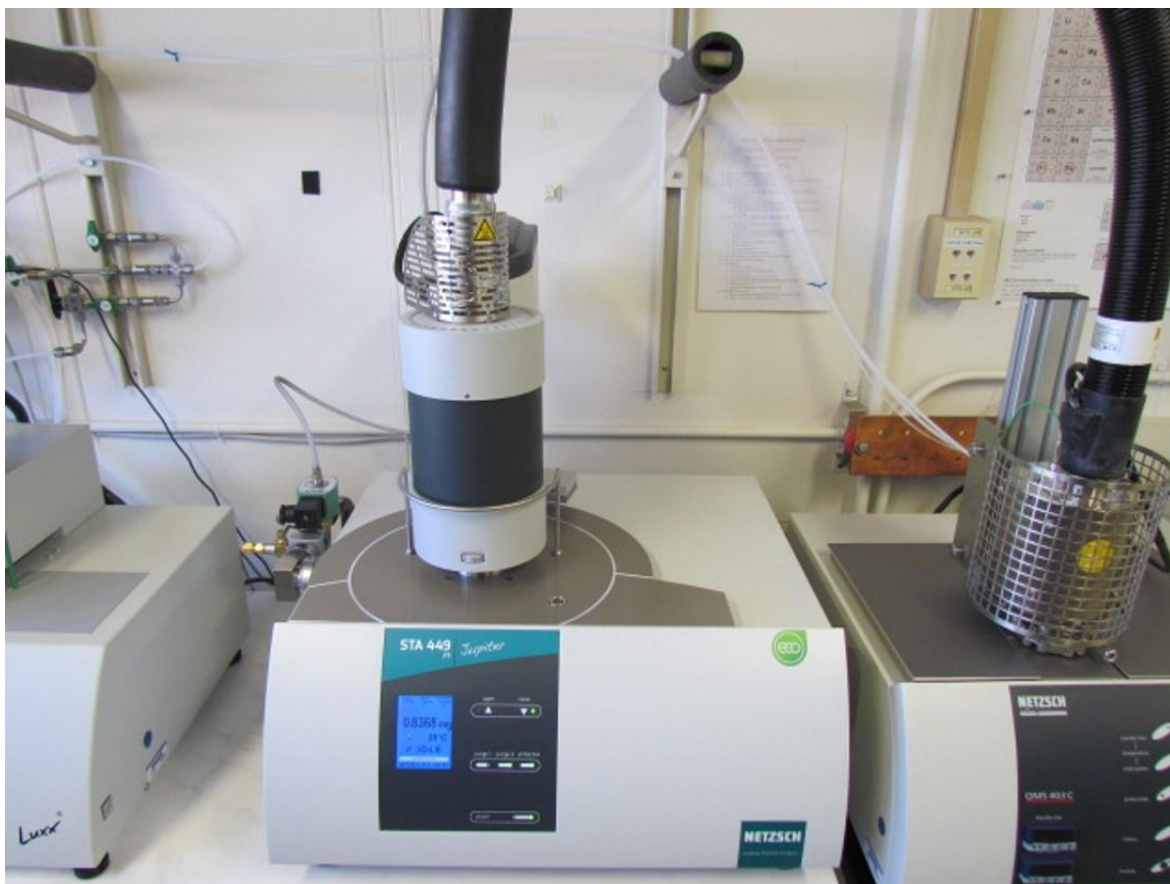


Figure 22. TGA-MS setup at LANL.

There are some key factors to consider when sintering metal powders including temperature, soak time, atmosphere, and ramp rate. These factors can influence the degree of densification and formation of various phases in the material. The sintering parameters were derived from thermal analysis technique thermogravimetric analysis (TGA NETZSCH STA 449 C Jupiter), to determine the optimal conditions for favorable particle coalescence. Mass spectroscopy is an addition capability of this thermal analysis tool. The TGA-MS is shown in Figure 22.



Figure 23. 1500°C MTI Muffle Furnace at UTEP.

An in-house MTI muffle furnace, shown in Figure 23. was used for atmospheric sintering. Commercial hot isostatic pressing was performed by American Isostatic Presses, Inc. Both processes were used to sinter the printed geometries for testing. The Virtual Foundry did not have a sintering protocol for the titanium grade 2 composite; however, it was recommended to start at 1350°C in argon atmosphere.



Figure 24. HIP setup at American Isostatic Presses [52].

The muffle furnace simply ramps to the prescribed temperature and at given temperatures the composite material will debind and sinter. The hot isostatic pressure furnace follows the sample heating progression but includes additional pressure to increase the consolidation of metal powders after debinding. The HIP setup at American Isostatic Presses is shown in Figure 24.

## 2.5 Corrosion Testing



Figure 25. Proteus Alpha Electrochemical Cell at LANL.

Corrosion resistance is an important property that corresponds to the in-service durability of bipolar plate due to operating in a corrosive environment. The corrosion resistance of the processed titanium is acquired and compared. The proteus alpha cell setup is designed to subject a sample to a given active area of electrolyte with temperature control as shown in Figure 25.

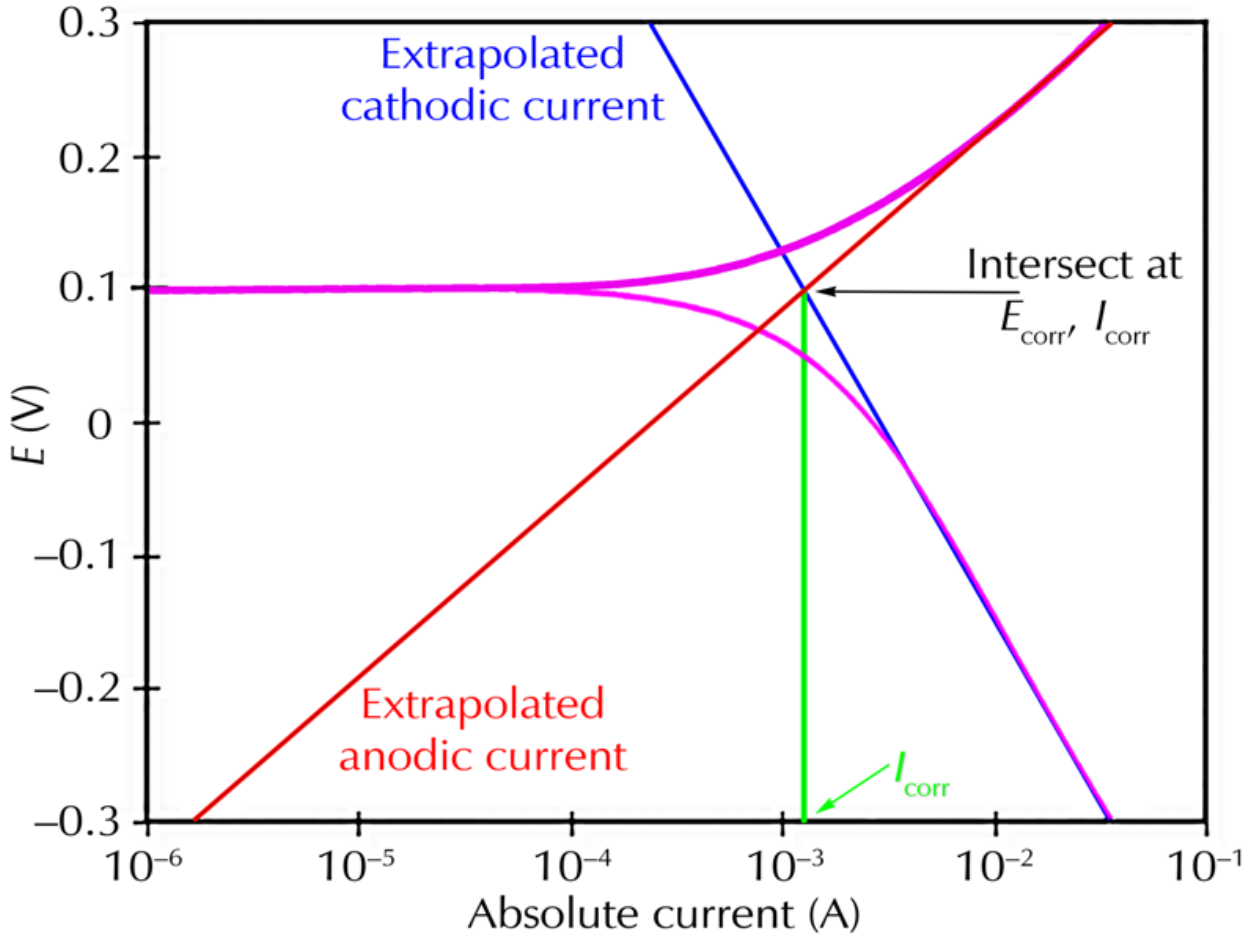


Figure 26. Tafel plot for corrosion [53].

The material will be subject to a potential range of 0.6V to -0.4V vs Ag/AgCl in an electrolyte that is pH 3 sulfuric acid at a temperature of 80°C. The outcome from this test is the corrosion current density which is obtained from the tafel plot as shown in Figure 26. The parameters of the corrosion test were selected from previous bipolar plate working groups at LANL and the DOE targets. However, there are various conditions that can be reported to evaluate the corrosion resistance that are present in the literature.

## 2.6 Hardness Testing



Figure 27. Buehler Hardness Tester at LANL.

The sintered materials will undergo hardness testing to evaluate the structural stability of the processed test specimen and compared to wrought titanium. This information is important due to common presence of porous and brittle materials because of post processing AM parts. The hardness tester is shown in Figure 27.

## 2.7 Summary

This chapter provided insight to the material and method of fabricating titanium composite components. Furthermore, the equipment was introduced that will be employed to subject the processed test specimens to BPP conditions. In the next chapter, the as-received material will be characterized to verify it as a titanium PLA composite material system.

## CHAPTER 3. MATERIAL CHARACTERIZATION

### 3.1 Introduction

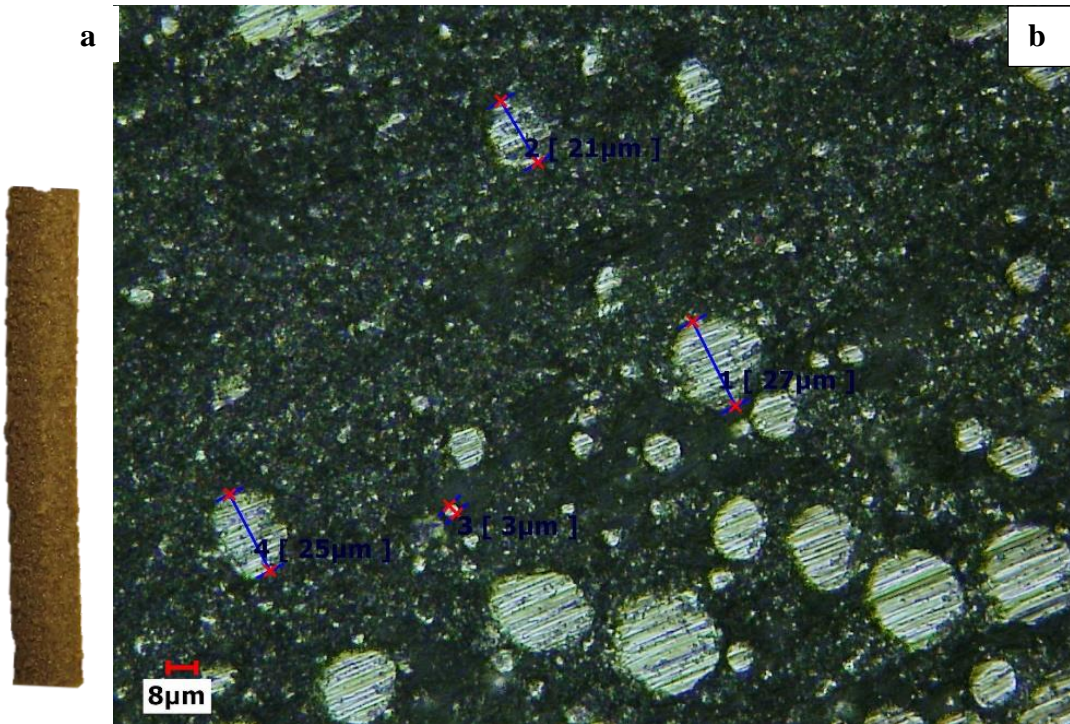


Figure 28. Optical Microscopy of Ti-grade 2 printed part (a) close-up of filament with 1.75 mm diameter (b) micrograph of visible Ti-grade 2 powder in the PLA matrix.

The subject material is characterized to verify the constituents and properties compared to the manufacturer claims. The material will be evaluated in as-received filament form as well as a printed geometry to execute specific characterization techniques. No special preparation has been performed outside of printing parts. In this chapter the following material characterization techniques are employed: scanning electron microscopy, energy dispersive x-ray spectroscopy, x-ray fluorescence, x-ray computed tomography, optical microscopy, optical profilometry, and thermogravimetric analysis mass spectroscopy. The feedstock filament with a 1.75 mm diameter and optical image of metal powder and PLA matrix is shown in Figure 28.

### 3.2 Scanning Electron Microscopy-Energy Dispersive X-ray Spectroscopy

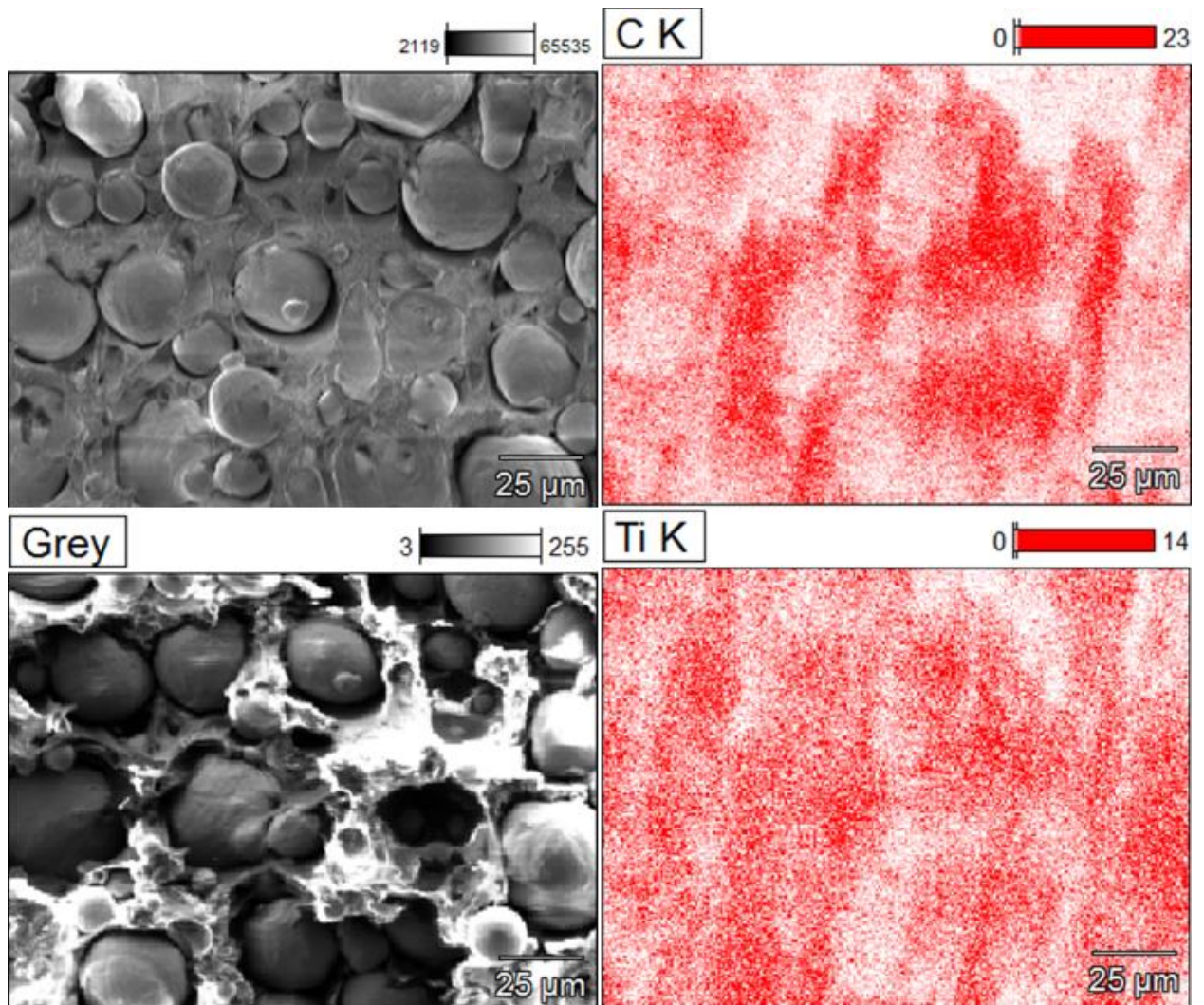


Figure 29. SEM and EDS of composite filament surface.

Scanning Electron Microscopy (SEM) is a visualization technique that produces images by scanning the surface with a focused beam of electrons. Furthermore, the electrons interact with atoms in the sample producing various signals that include composition information. This tool is known as energy-dispersive x-ray spectroscopy (EDS). SEM and EDS is used to take a closer observation of the material surface and characterize the elements present as features appear with environmental changes. SEM was used to evaluate the microstructure of the composite filament

surface and perform elemental mapping to display the presence of each element. The expected elements titanium and carbon were present is the predicted locations of the filament surface. Figure 29 illustrates the surface distribution of titanium powder and PLA matrix with the respective elemental mapping.

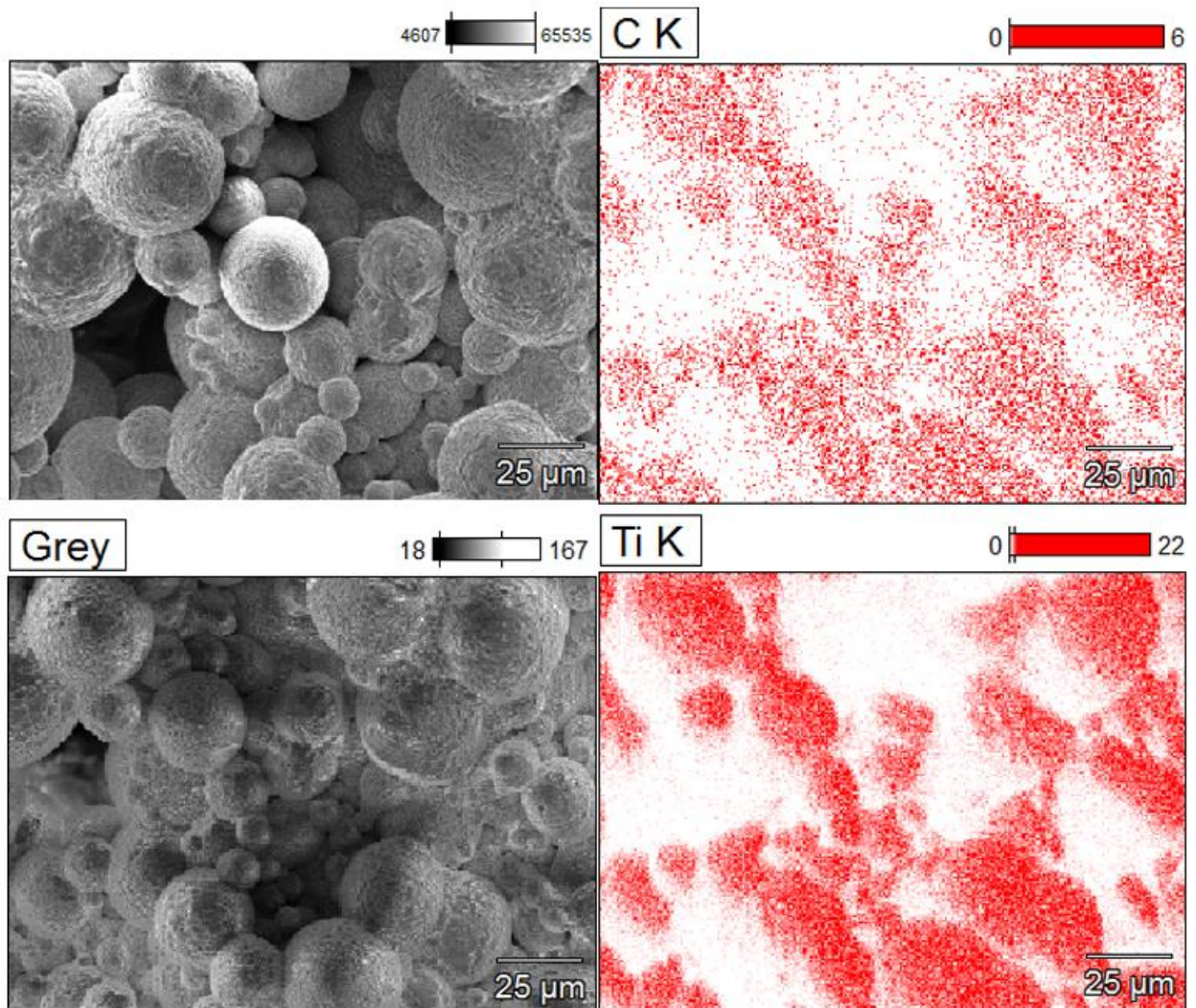


Figure 30. SEM and EDS of the sintered composite filament surface.

The material distribution of the composite filament surface is apparent. However, more information is needed to determine if this distribution is consistent through the cross-section. SEM images of the post sintered composite material were also obtained as shown in Figure 30. The

corresponding EDS mapping showing an increase in titanium counts and decrease in carbon counts supports the notion that the PLA has been thermally degraded.

### 3.3 X-ray Fluorescence

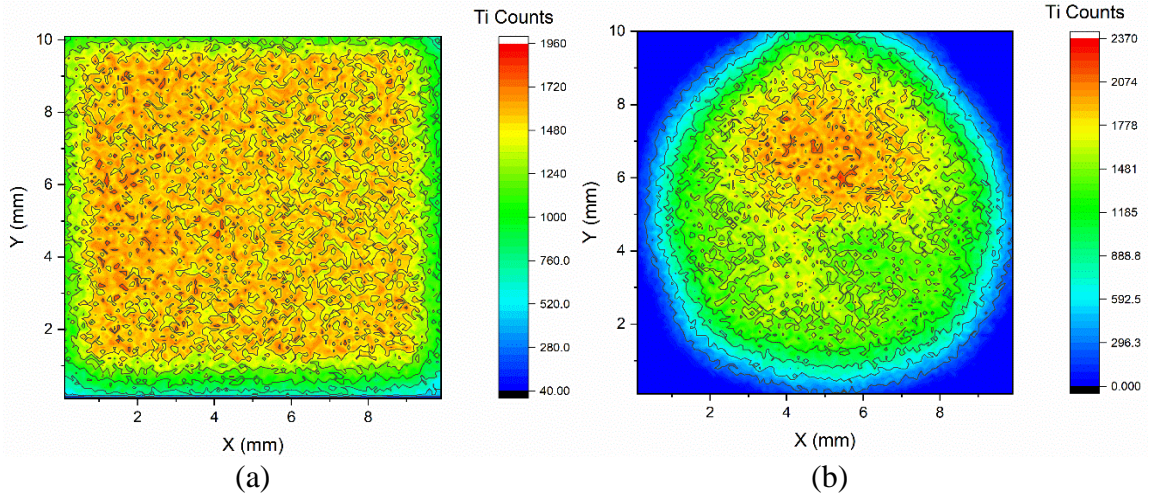


Figure 31. XRF mapping of printed material (a) before and (b) post debinding and sintering.

X-ray fluorescence (XRF) is an elemental analysis method where a subject material is excited with high-energy x-rays and the emission of characteristic secondary x-rays are used to quantify the elemental composition. XRF was used to confirm the metal composition of the feedstock filament. According to the XRF report, the element is 100% titanium. XRF mapping, shown in Figure 31(a) confirmed the present metal powder as titanium and the distribution across the surface area. The PLA was unable to be directly quantified via XRF because of the energy levels of carbon, hydrogen, and oxygen are below the detectable limits, so the lower counts of titanium are associated with increased presence of PLA. XRF mapping of the post sintered composite material showed an increase in titanium spatial proximity and counts meaning there was a reduction in the PLA presence illustrated in Figure 31(b). The mapping information was consistent with the degree of metal powder coalescence shown in the SEM image shown in Figure

30 The SEM data shows complete metal powder coalescence at the surface in addition to non-uniform porosity.

### 3.4 X-ray Computed Tomography

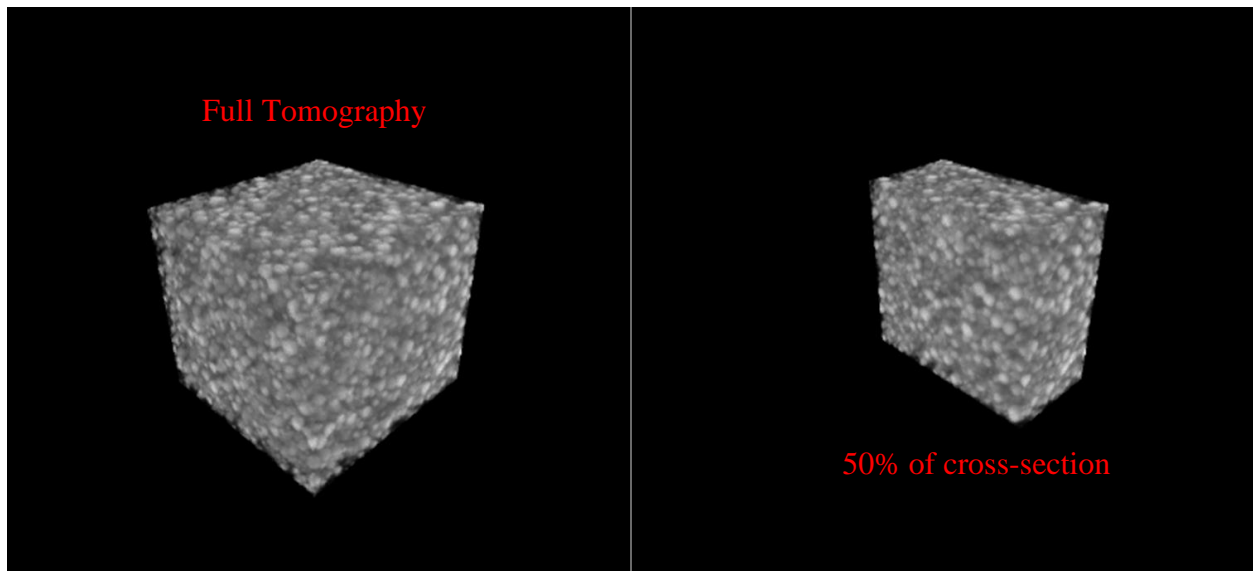


Figure 32. Full tomography and 50% of composite filament cross-section via XCT.

X-ray computed tomography (XCT) is another x-ray-based characterization tool where 360° attenuated signals are detected to reconstruct the internal features of the specimen cross-section. This technique can be used to qualify or quantify the distribution and dimensions of features and materials. XCT is employed to reveal that the distribution of metal powder is consistent through cross section of the as-received filament as shown in Figure 32. Attenuated x-rays detected after penetration show the contrast difference in the higher atomic mass of the titanium powders compared to the PLA matrix.

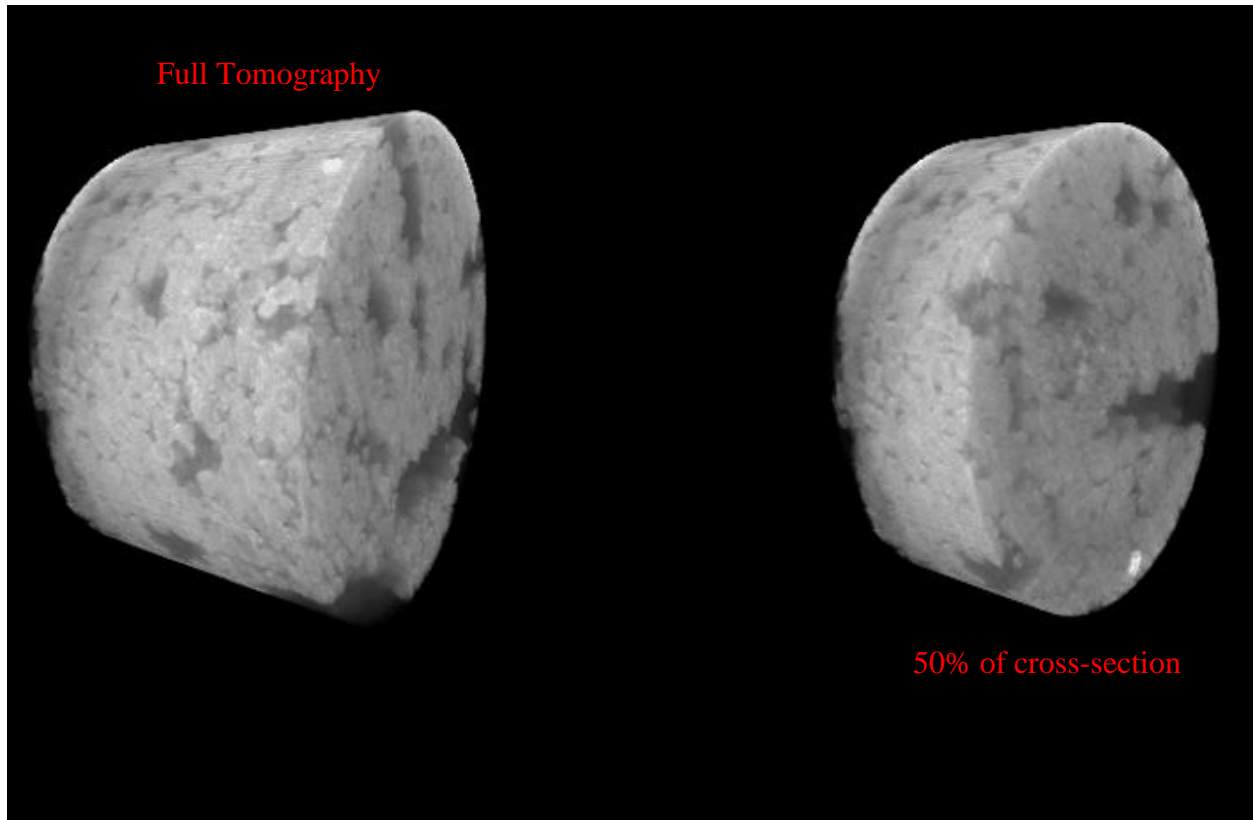


Figure 33. Full tomography and 50% of composite filament post sintering.

XCT also characterized the composite filament post sintering as shown in Figure 33. The PLA matrix is evacuated, and the titanium powders are closer in proximity. Porosity is apparent in the full tomography and is consistent throughout the cross-section.

### 3.5 Optical Profilometry

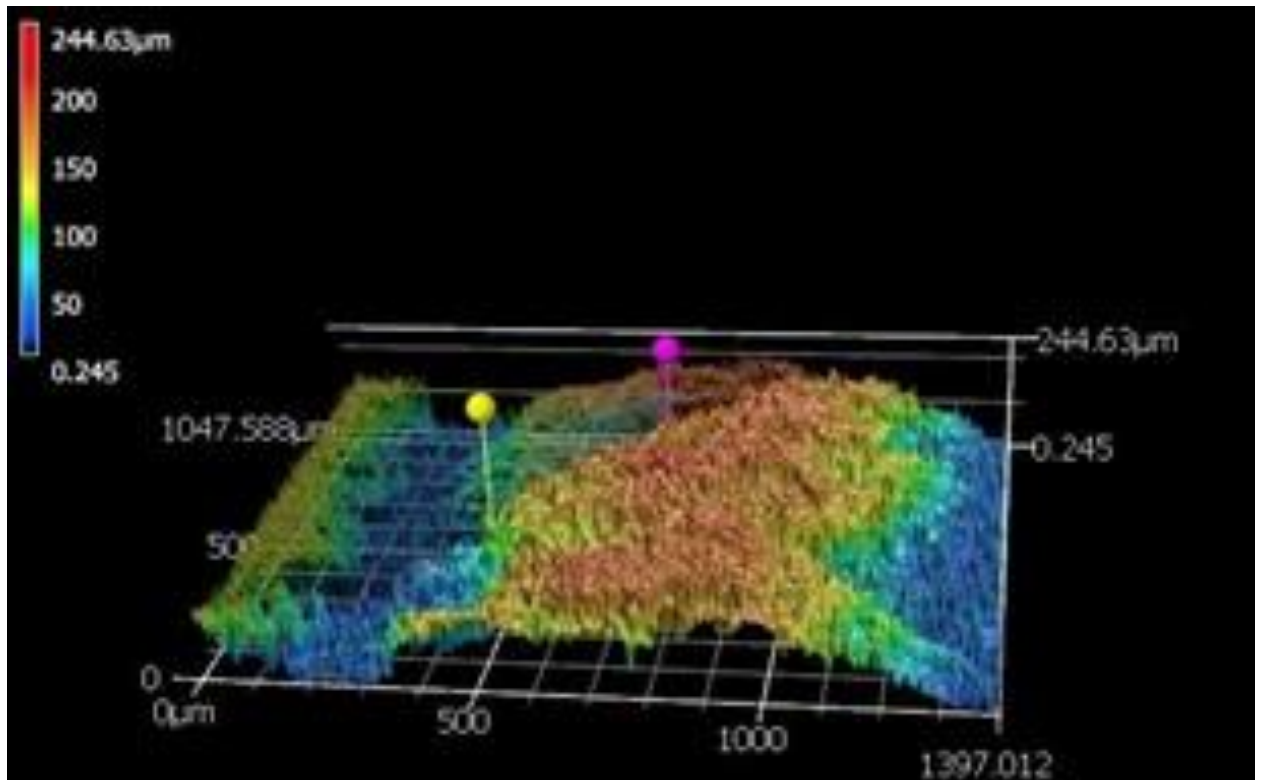


Figure 34. 3D roughness profile of as-received composite filament

Optical Profilometry (OP) is a non-contact method used to extract topographical data from a surface. OP tracks the evolution in surface roughness as the material changes. Surface roughness is an important parameter that is associated with electrical properties regarding potential contact points and wettability properties for water mobility of the bipolar plate. It is important to capture the evolution of surface roughness throughout the AM process so this information can be correlated to the performance values later in the study. The surface roughness evolution will also provide information regarding the quality of sintering. OP provided information on the roughness evolution of the composite material. Figure 34 illustrates the 3D topography of the as-received filament.

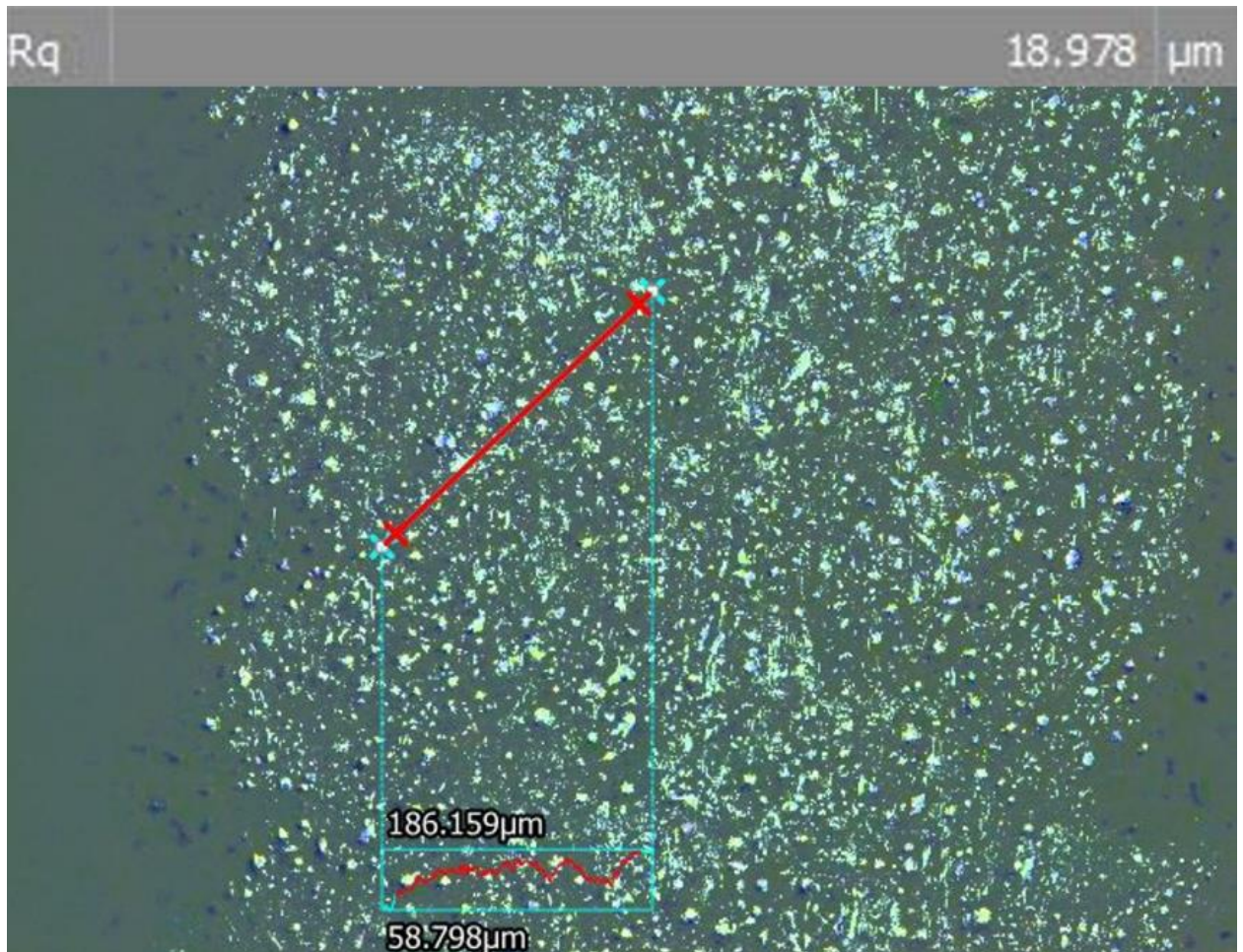


Figure 35. Profilometry of as-received composite filament with roughness values.

Figure 35. shows the line scan of the composite filament with corresponding surface roughness value of 19  $\mu\text{m}$ . The roughness of the as-received filament is mostly considering the height differences between the PLA and the metal powders. This does not provide insight to the performance of the material as a bipolar plate until it is thermally processed, so it serves as a baseline to the roughness evolution.

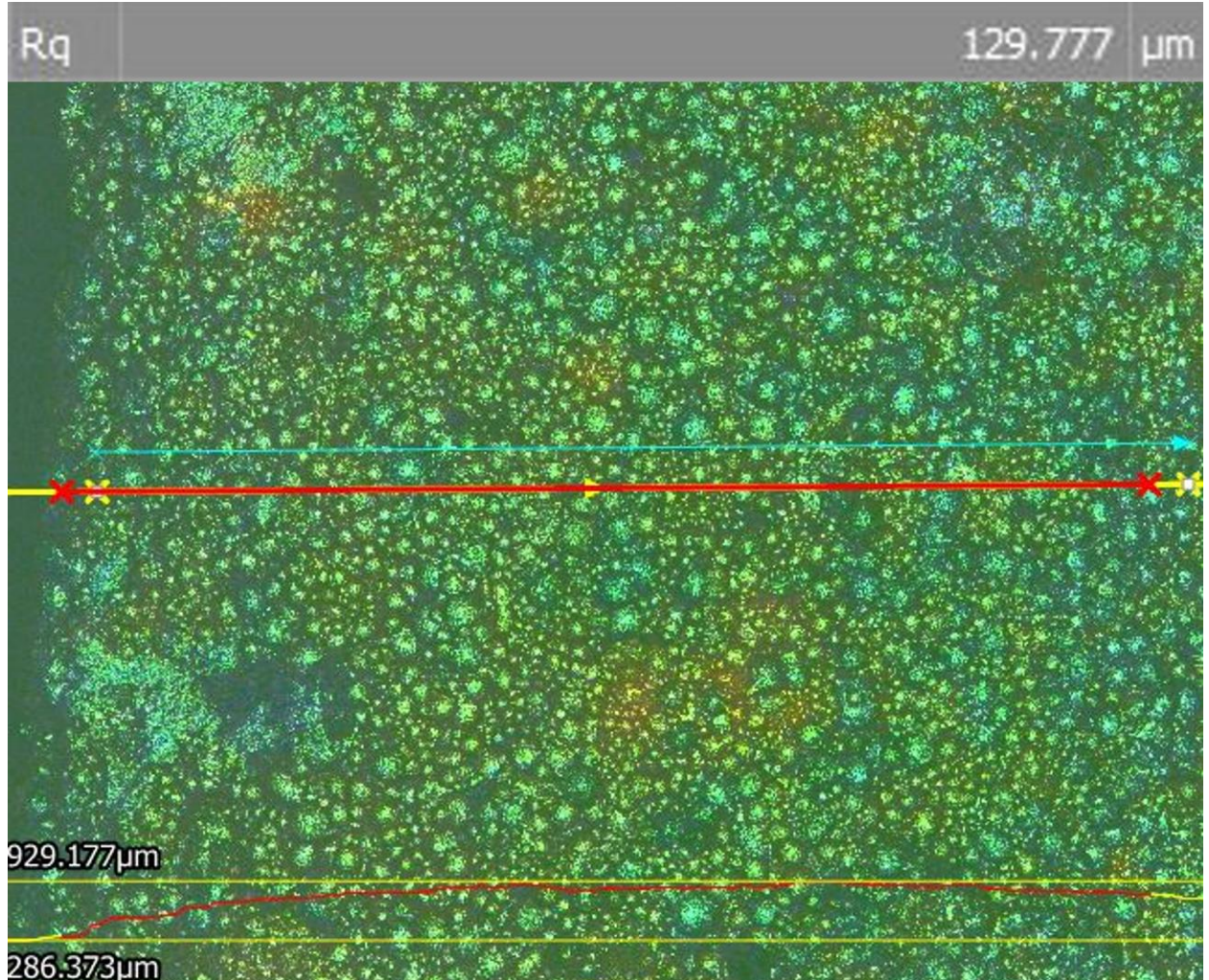


Figure 36. Profilometry of post sintered composite filament with roughness values.

The roughness of the post sintered sample increased from the baseline as-received sample as shown in Figure 36. This increase in roughness to 130  $\mu\text{m}$  is attributed to the grain growth of the titanium powders. As the metal powder begin to sinter, the grains become increasingly coarse which creates more elevation changes at the surface and increase the amount of grain boundaries. Also note that this grain coarsening is not uniform in addition the range of particle sizes which explains the surface elevation changes. The topography of the post sintered composite filament is shown in Figure 37.

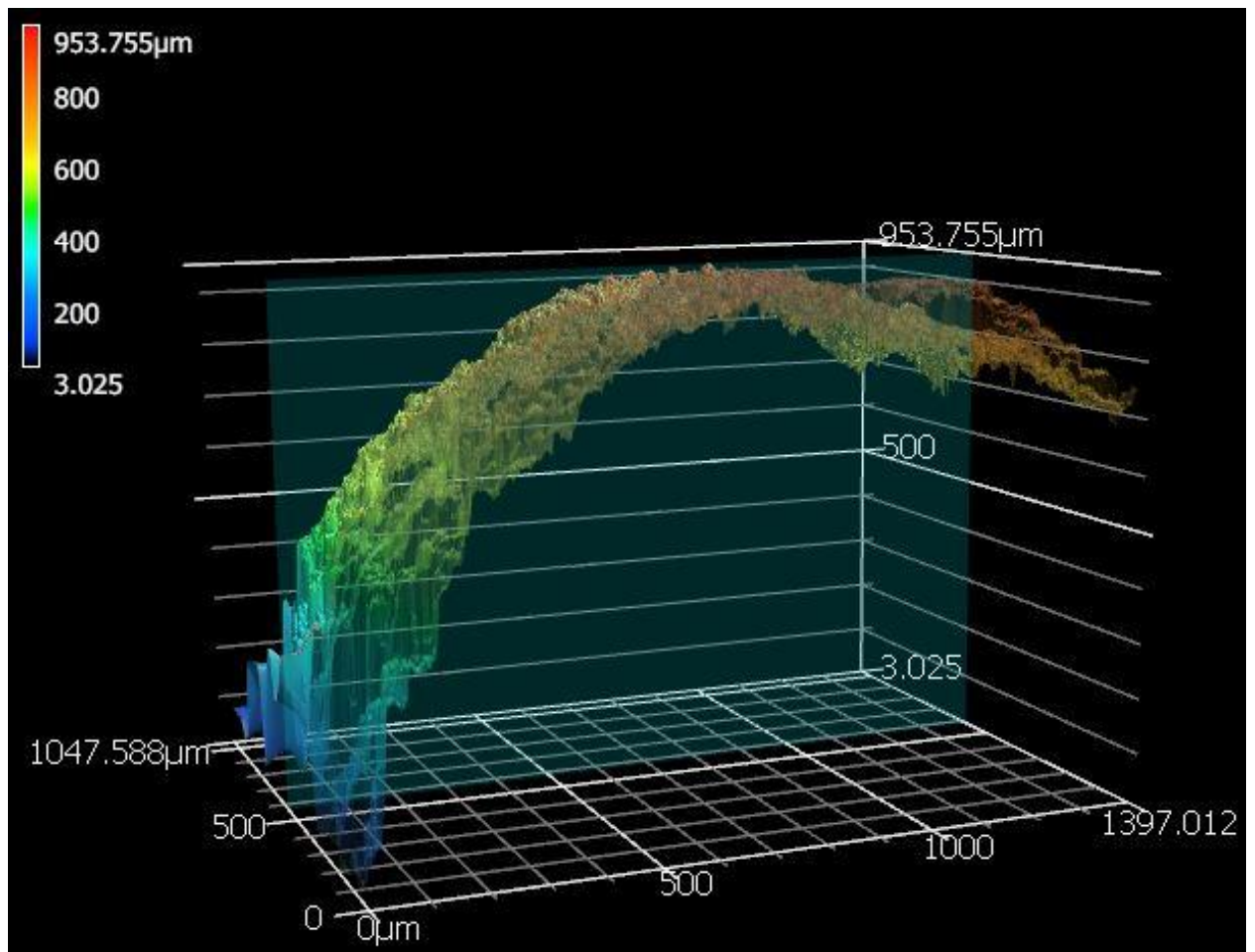


Figure 37. 3D roughness profile of sintered composite filament.

### 3.6 Thermogravimetric Analysis- Mass Spectroscopy

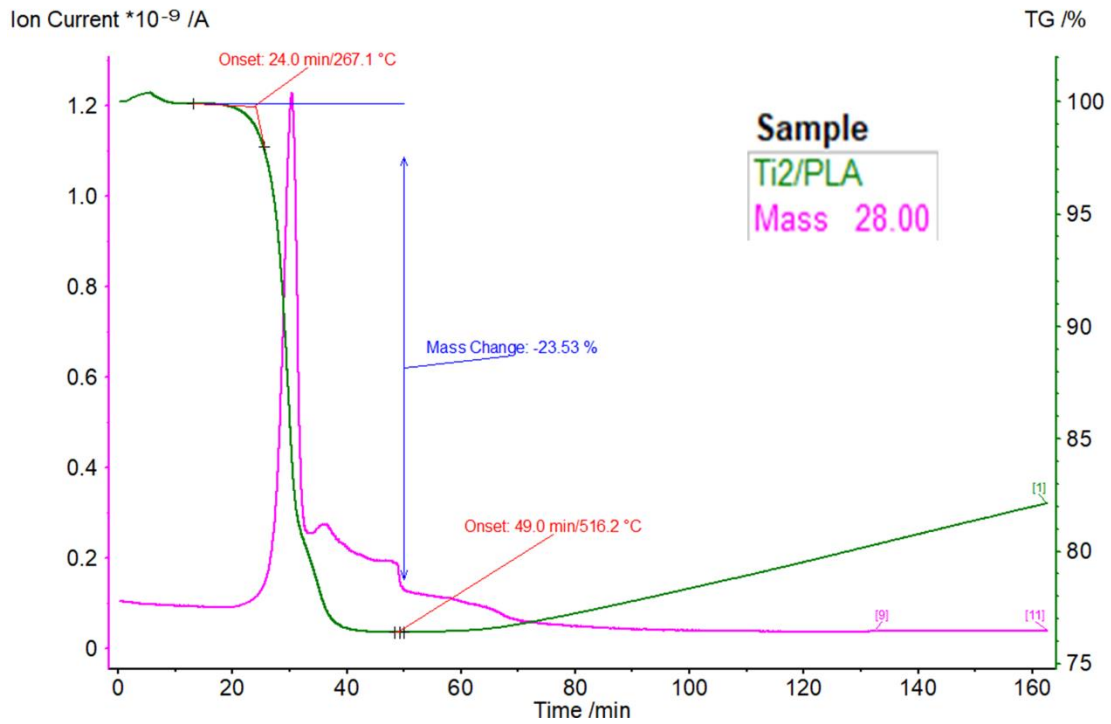


Figure 38. TGA-MS of the composite filament at 1400°C.

TGA is an analytical technique used to determine the thermal stability of a material by measuring the weight change as a function of temperature. This analysis tool provided the conditions in which the PLA totally degrades. Mass spectroscopy is a supplementary tool to analyze the PLA elements as it degrades. This provides insight into what molecules the PLA decomposes into. The mass loss percentage of 23.53% is shown to confirm the manufacture claim of 76% metal powder and 24% PLA binder as shown in Figure 38. Additionally, the mass spectrometer shows carbon monoxide peak as the dominant species of the PLA decomposition.

### 3.7 Summary

In this chapter, the material characterization was performed to verify the commercial material as titanium for the next steps to process in optimized conditions and test the processed

material for BPP characterization. In the next chapter the sintering optimization study will commence to down-select the best conditions for sintering the titanium composite.

## CHAPTER 4. SINTERING OPTIMIZATION

### 4.1 SEM Characterization

This chapter will show the sintering progression of the titanium composite filament at various temperatures and the verification of the optimized temperature against printed geometries. The dimensions of the printed cube are 10 mm x 10 mm x 5 mm, while the printed disc has a diameter of 10 mm and a thickness of 3 mm. The atmosphere for each run is argon with a ramp rate of 30°C/min.

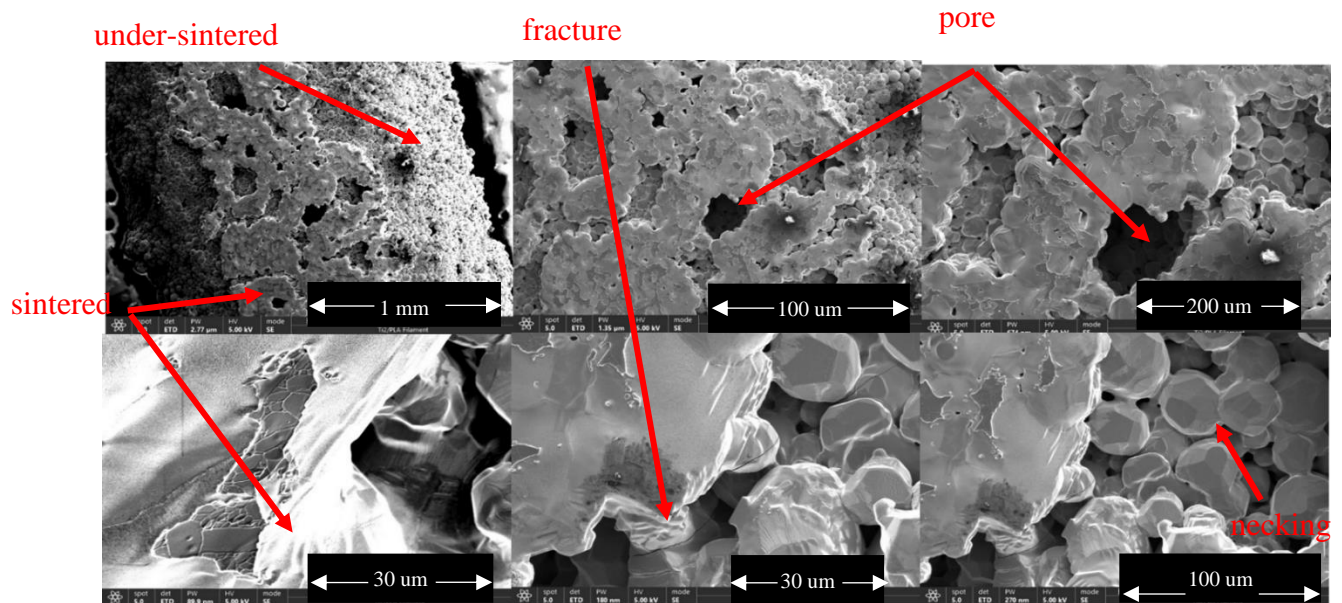


Figure 39. Sintering at 1350°C as recommended by the Virtual Foundry.

The Virtual Foundry metal composite filament manufacturer typically provides sintering protocol for each feedstock filament they sell. However, regarding titanium, there is not an available thermal process to achieve quality sintering. The manufacturer suggestion is to begin with a sintering temperature of 1350°C Titanium is a complicated material to process due to its intense affinity for oxygen. Per the suggestion, the sintering optimization begins at 1350°C. As shown in Figure 39, the filament contains an array of features that indicate sintering does

commence at 1350°C. Apparent regions of necking are present in the micrographs in addition to areas where the titanium is fully sintered. The sintered regions are represented by a smooth microstructure. Accompanying the sintering features are regions of under-sintering, internal and external to the titanium particles. Under-sintering is when the particles increase in proximity but do not actually transition to a single structure. The external under-sintering is represented by grain coarsening of the metal powders. The internal under-sintering is represented by fracture surfaces with a textured finish.

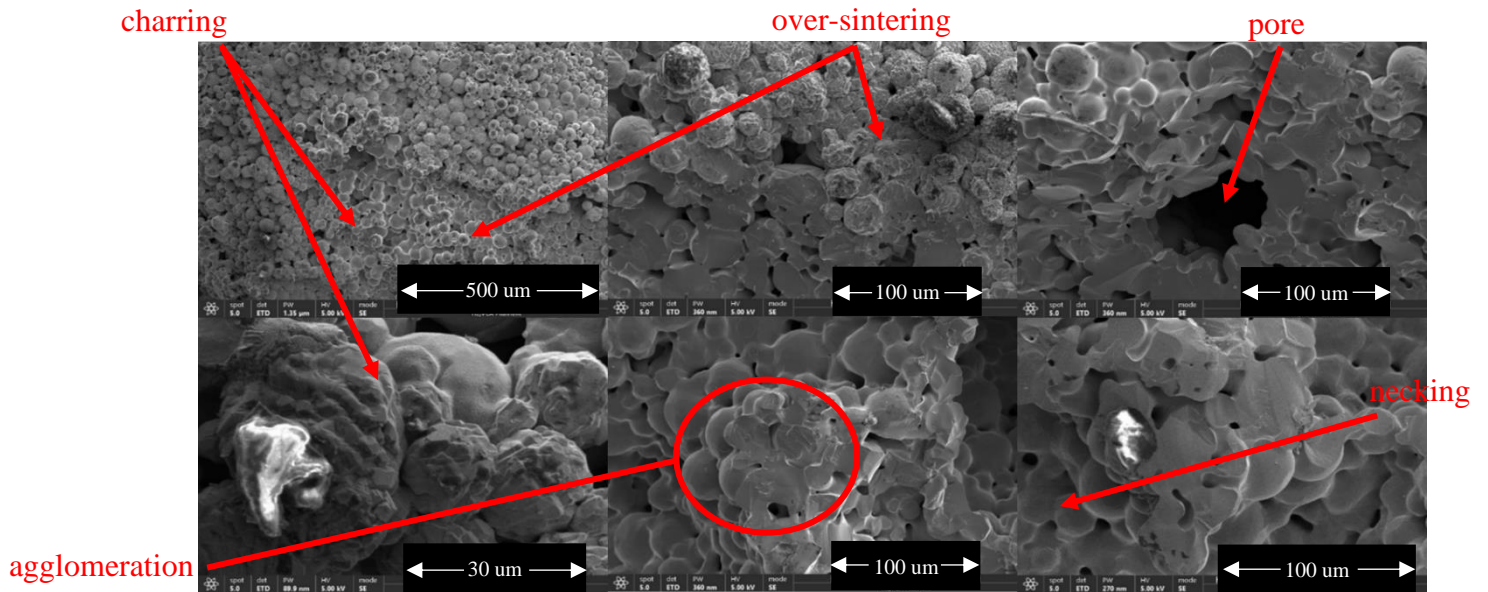


Figure 40. Over-sintering of the titanium filament at 1450°C.

The attempt to sinter the titanium at 1450°C resulted in over-sintering as shown in Figure 40. The over-sintering is observed based on the lackluster finish of the coalesced powders and necking features. There is charring of the PLA observed in the micrographs. This is due to the separation of the carbon monoxide molecule resulting in a residual carbon-based soot that redeposited on the powder surface. Irrespective of the over-sintering an agglomeration is also observed. This is due to the range of powder particle sizes in a proximal region. The smaller

particles are absorbed by the larger ones and the process repeats. This can result in clusters of metal powders with internal and external porosity.

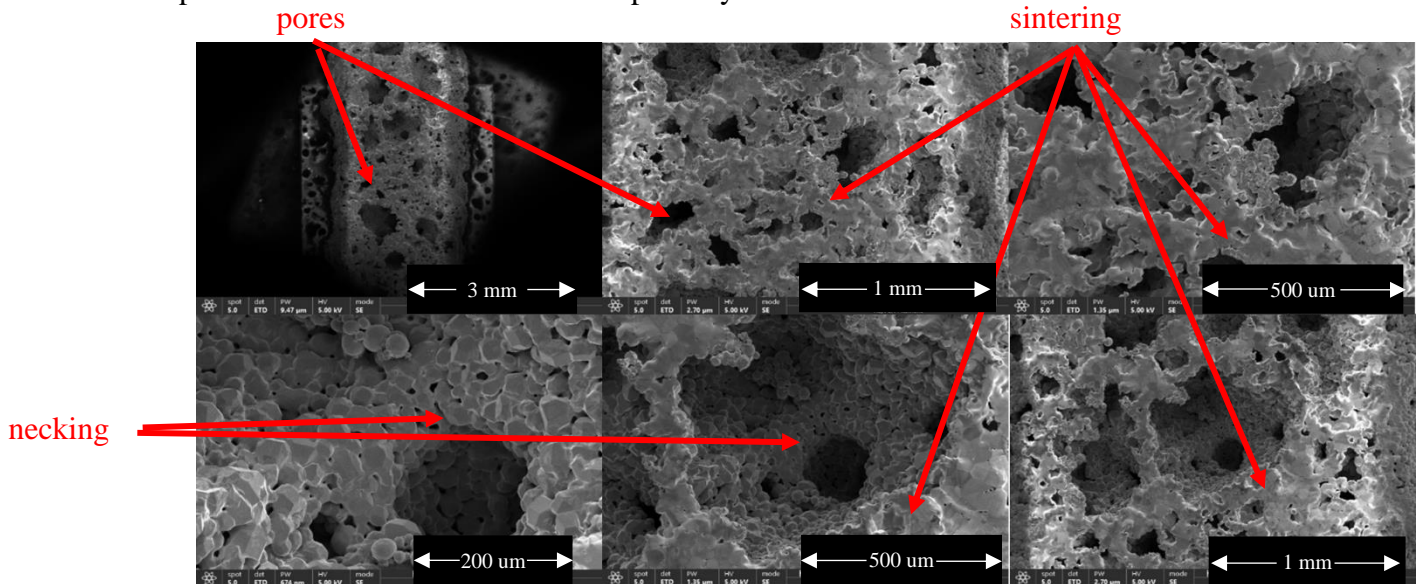


Figure 41. Sintering of the titanium filament at 1400°C

Sintering of the titanium at 1400°C resulted in a well dispersed sinter profile of the composite filament shown in Figure 41. Sintering features, both necking and full coalescence, are observed at the surface and sub-surface in the cavern-like structures. The obvious porosity is due to the ratio of metal content to the PLA binder and the proximity of neighboring particles. The sintering temperature is proven to achieve adequate sintering of the filament. Additional optimization is necessary to see if the temperature can be applied to a printed geometry. Also layering the filament in smaller widths can increase the proximity of metal powders to reduce the porosity.

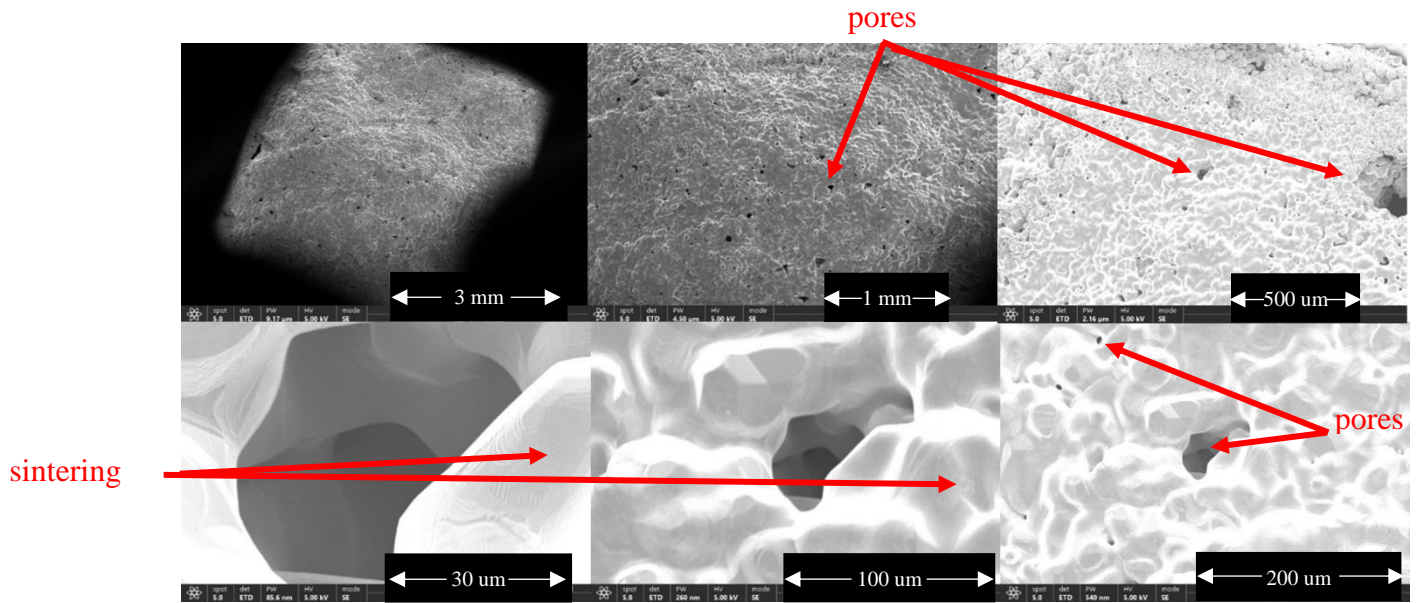


Figure 42. Sintering of printed cube at 1400°C

Sintering of the printed cube at 1400°C resulted in a smooth cohesive microstructure with a reduction in porosity at the surface as shown in Figure 42. Sufficient powder coalescence and sintering is apparent across the surface of the cube. However, there are still local pores remaining despite the porosity reduction compared to the sintered titanium filament. The sintering temperature results are sufficient for the filament and the printed cube. An additional geometry, printed disc, will be sintered to further evaluate the temperature parameter.

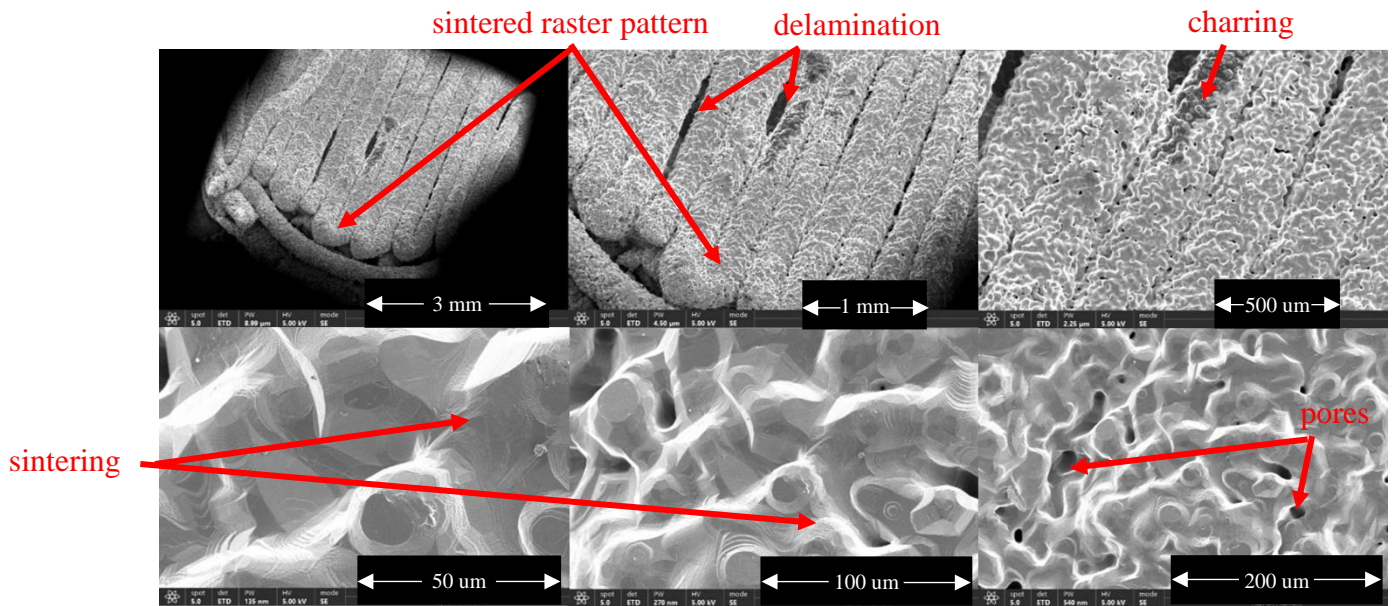


Figure 43. Sintering of printed disc at 1400°C

Sintering of the printed disc performed at 1400°C with a smooth microstructure and porosity is shown in Figure 43. The raster pattern is observed to be sintering in its original position which shows the opportunity to create passive water management geometries and sinter them in position. There are regions of delamination between adjacent print layers and some charring from the carbon-based soot. The porosity is not as prolific compared to the sintered cube. The sintering temperature is confirmed to produce quality results at 1400°C.

## CHAPTER 5. POST PROCESSING OF PRINTED TEST SPECIMEN

Chapter 5 will cover the processing of the printed test specimen using commercial HIP and thermal sintering via a novel technique. The conditions for the commercial HIP samples are sintering temperature 1400°C with an input pressure of 80 MPa and atmospheres of argon and air. The conditions for the thermal sintering are sintering temperature 1400°C in atmospheres nitrogen and air. The test specimens are a 30 mm x 30 mm x 30 mm cube, 30 mm x 30 mm x 6 mm plates, and 30 mm x 30 mm x 3 mm plates.

### 5.1 Hot Isostatic Pressing



Figure 44. HIP of test specimen at 1400°C in air.

The test specimen sintered in the HIP furnace were not usable for BPP characterization as shown in Figure 44. Due to being exposed to nitrogen and oxygen, the specimen became severely brittle and disintegrated at the onset of physical touch. These conditions are not suitable for sintering of the titanium composite test specimen.



Figure 45. HIP of the test specimen at 1400°C in argon.

The test specimens were sintered in the HIP furnace with an argon atmosphere as shown in Figure 45. Unlike the specimen that were sintered in air, there is structural integrity, so the materials were able to be handled. However, the applied pressure caused severe warping. The brown part post de-binding is not stable enough to endure pressure assisted sintering. Sintering in ambient pressure allows for the powders to adequately coalesce before being subjected to additional pressure. There is also apparent porosity on the sides of the sintered cube.

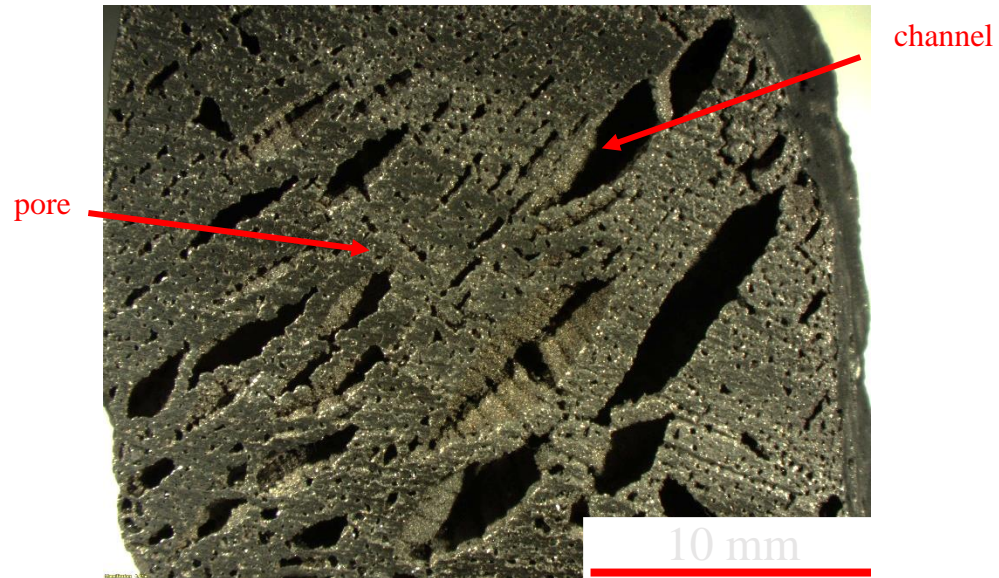


Figure 46. Machined HIP sintered cube at 1400°C.

In addition to the porosity on the sides of the cube, there are pores and channels inside as well as shown in Figure 46. The internal cross section also shows that the cube has been successfully sintered. The input pressure further assisted the coalescence of neighboring metal powders. This also contributed to formation of channels throughout the cross-section. This specimen is suitable for BPP characterization.

## 5.2 Thermal Sintering

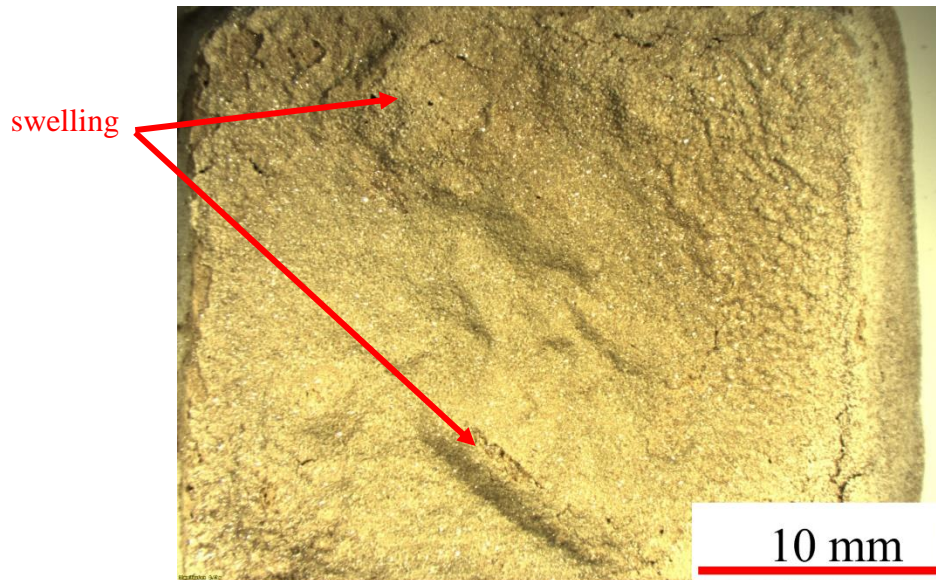


Figure 47. Thermal sintering of printed plate at 1400°C in air.

Contrary to the HIP cube sintered in air, the processed plate maintains its structural stability as shown in Figure 47. There is some apparent swelling where the vaporized PLA was inhibited from fully escaping. This swelling feature is common in mixed material systems with varying sintering temperatures and particle sizes. The thermal degradation temperature of the PLA produces a vapor that attempts to escape through the interstitial metal particles. When the particles vary in size PLA can become trapped beneath larger metal particles. It is important to note that dimensions of the plate increased from 29.85 mm x 29.90 mm x 5.93 mm to 34.62 mm x 35.09 mm x 8.34 mm. The largest increase ensued in the x and y direction compared to the z. Due to excessive oxidation this sample is not suitable for BPP characterization.

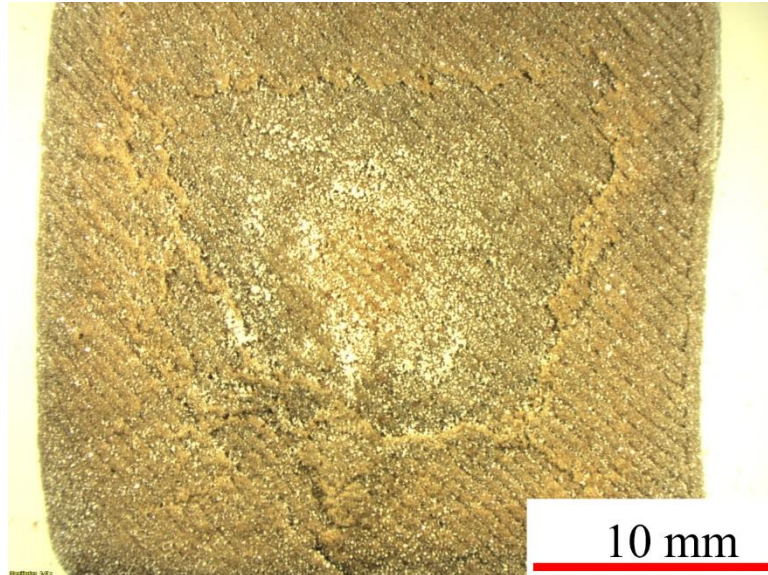


Figure 48. Sintering of printed plate at 1400°C in nitrogen.

The plate thermally sintered in nitrogen showed a more controlled process of oxide formation as shown in Figure 48. The raster pattern of the printed plate is still visible which supports the notion of controlled oxidation growth. The nitrogen gas is the tuning factor due to it being an inert and having the capacity to displace oxygen. The combination of the carbon monoxide shield and the nitrogen atmosphere presents the opportunity to create oxide layers for added corrosion resistance. The sintered specimen also maintained good dimensionality by increasing from 29.75 mm x 29.70 mm x 3 mm to 30.00 mm x 30.06 mm x 5.20 mm. The greatest increase in dimension occurred in the z direction. This thermally sintered specimen is suitable for BPP characterization testing.

### 5.3 Summary

It has been shown that the test specimen can be sintered in multiple atmospheres, argon, nitrogen, and air. It is observed the test specimen maintain a sense of dimensionality which is important when it comes to existing capabilities into existing systems. A key takeaway from this chapter is the revelation of tunable oxide layer growth which is advantageous in a corrosive

environment. In the next chapter, the processed test samples will be tested in the context of BPP conditions to gauge the effects on the titanium composite material.

## CHAPTER 6. BIPOLAR PLATE CHARACTERIZATION

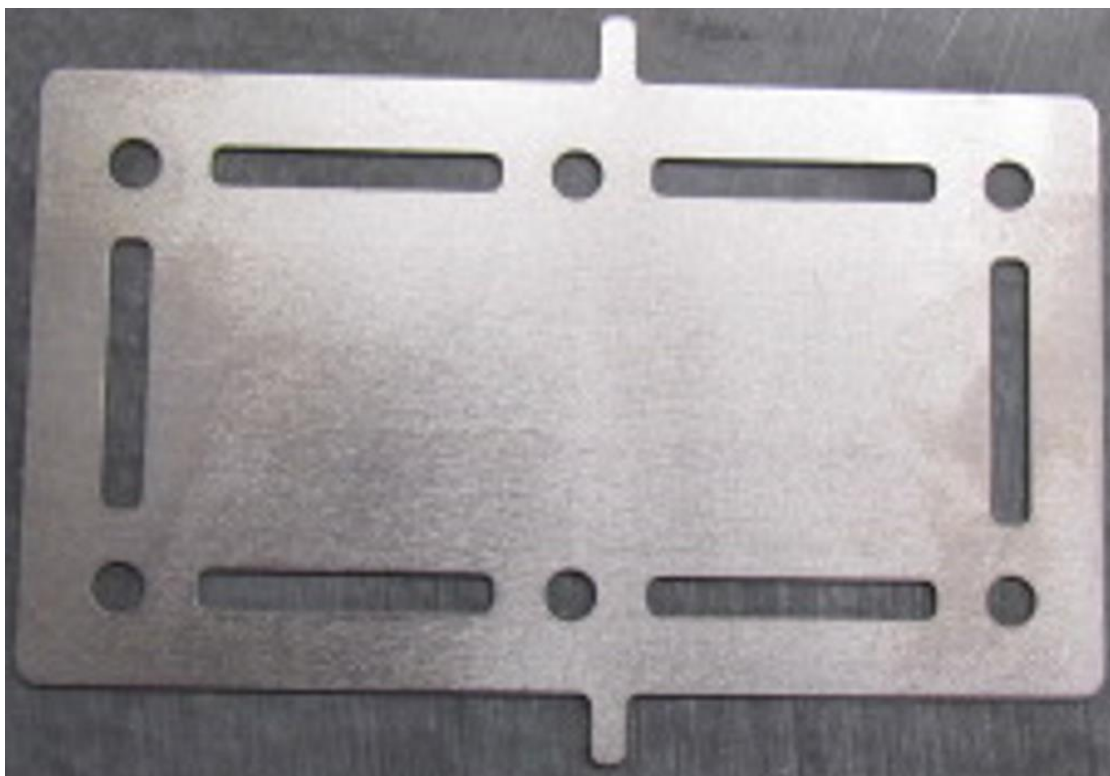


Figure 49. Baseline BPP used in PEFC stack at LANL.

Chapter 6 will cover the bipolar plate characterization utilizing corrosion testing, area specific resistance measurements, and electrical conductivity measurements. These results will be compared to the 2030 DOE targets for bipolar plates. Supplementary techniques will be implemented to investigate additional material properties. These techniques include optical profilometry to characterize the surface roughness and EDS to observe what elements are present post-processing. These properties including the DOE targets will be compared to a baseline titanium grade 2 bipolar plate. The DOE targets with the properties of interest are shown in Table 3. This baseline BPP is traditionally manufactured, its dimensions are 71.17 mm x 40.62 mm x 0.53 mm and is currently used in PEFC stacks at LANL. The baseline BPP is shown in Figure 49.

Table 3. 2030 DOE targets for BPP [54].

Characteristic	Units	2030 Targets
Cost	\$/kW <sub>net</sub>	5
Durability	hrs	25,000
Plate weight	kg/kW <sub>net</sub>	<0.18
Plate H <sub>2</sub> Permeation Coefficient	std cm <sup>3</sup> /(sec cm <sup>2</sup> Pa) @ 80°C, 3 atm, 10%Rh	<2X10 <sup>-6</sup>
*Corrosion anode	μA/cm <sup>2</sup>	<1 and no active peak
*Corrosion cathode	μA/cm <sup>2</sup>	<1
*Electrical conductivity	S/cm	>100
*Area specific resistance	ohm cm <sup>2</sup>	<0.01
Flexural strength	MPa	>40
Forming elongation	%	40

### 6.1 Optical Profilometry

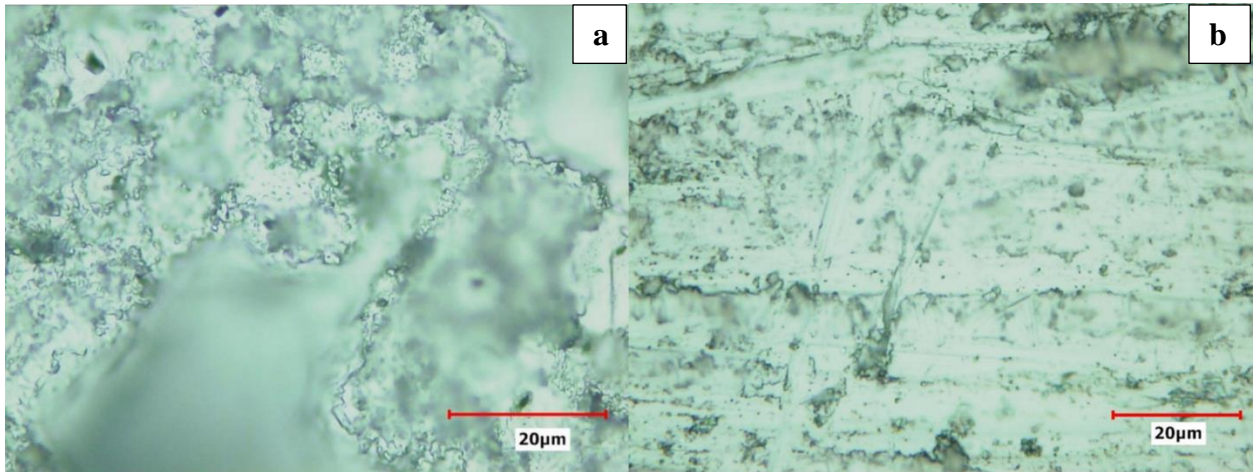


Figure 50. Optical microscopy of the (a) HIP cube vs. the (b) baseline BPP.

The root mean square surface roughness parameter Sq was evaluated for the HIP cube and the baseline BPP. The optical images for both samples are shown in Figure 50. The surface roughness value for the HIP cube and the baseline BPP are nearly identical, 1.146 for the HIP cube and 1.149 for the baseline BPP.

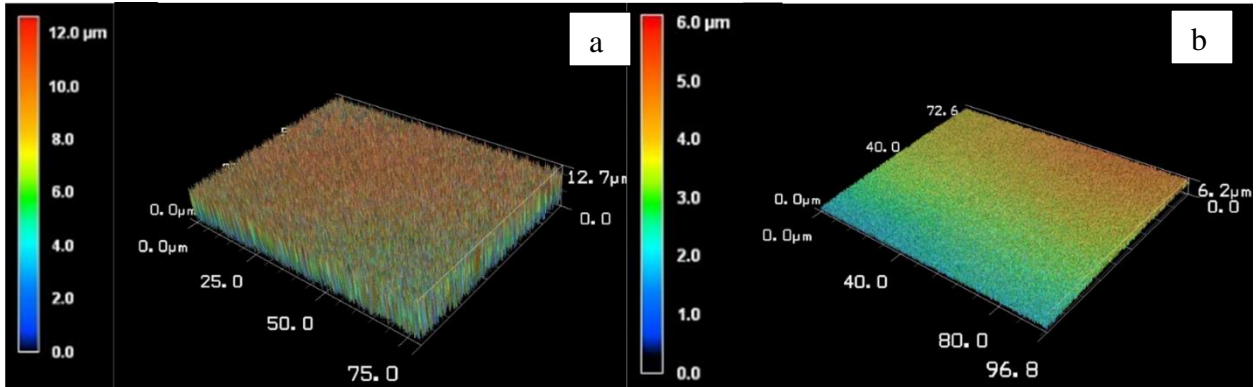


Figure 51. Topography of the (a) HIP cube vs. the (b) baseline BPP.

The topography of the HIP cube and the baseline BPP has been acquired and compared as shown in Figure 51. Despite the two samples having nearly the same surface roughness, the HIP cube has a higher mean height. This is due to the layered nature of material extrusion AM parts. The mean height for the HIP cube is 12  $\mu\text{m}$  while it is only 6  $\mu\text{m}$  for the baseline BPP. The topology of the baseline BPP is also showing a gradient with a linear relationship.

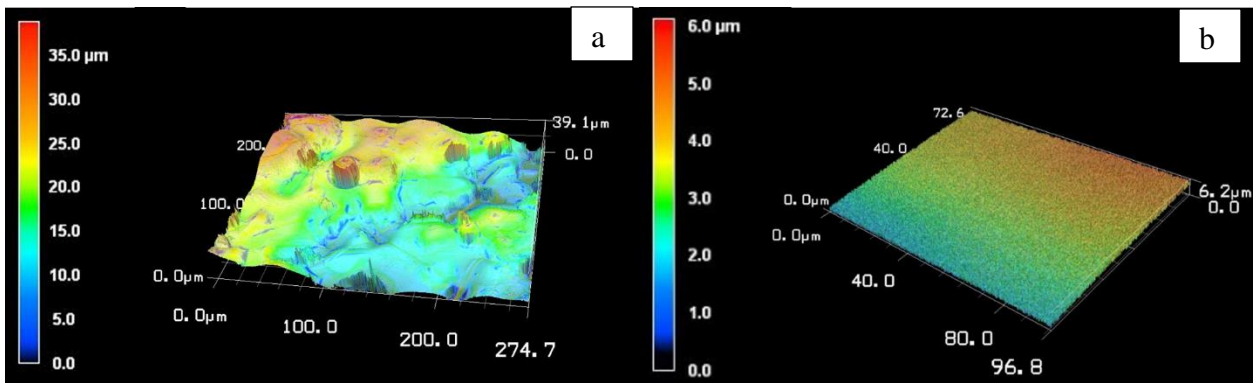


Figure 52. Topography of (a) thermal sintered Ar and (b) baseline BPP.

The topography of the thermal sintered specimen in argon and baseline BPP is compared as shown in Figure 52. This sample has an apparent rougher surface compared to the baseline BPP. The prominent peaks on the thermal sintered argon surface can lead to increased contact points for conductivity in a metal to metal configuration.

## 6.2 Energy Dispersive X-ray Spectroscopy

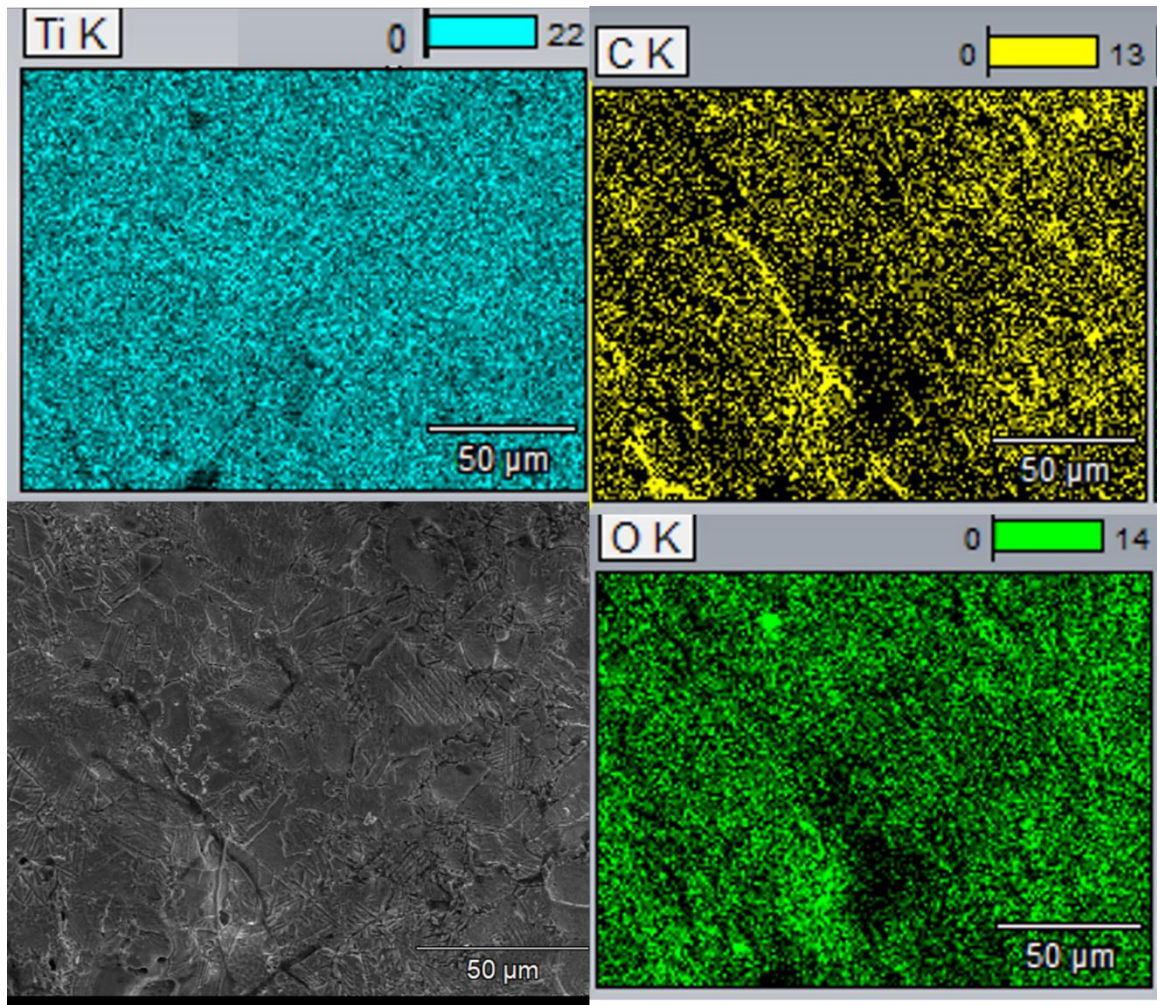


Figure 53. EDS mapping of the HIP cube.

The EDS map of the HIP cube processed in argon has been obtained as shown in Figure 53. The sample is predominately titanium due to the inert environment during sintering. The presence of carbon is also detected, and this is from the PLA binder which is carbon-based.

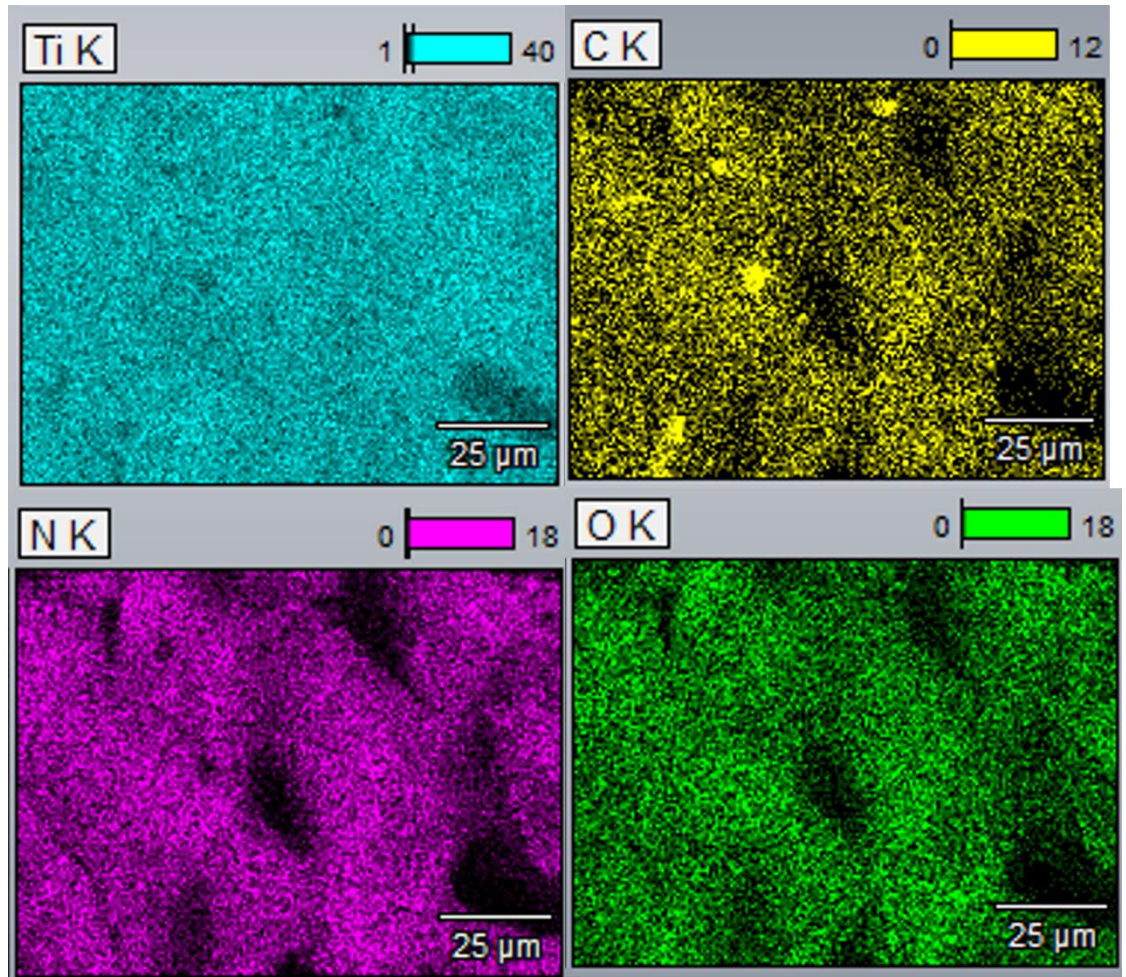


Figure 54. EDS mapping of thermal sintered in Argon specimen.

The EDS map of the thermal sintered in argon specimen has been acquired as shown in Figure 54. Similar to the HIP cube, a presence of carbon and oxygen is detected. The presence of nitrogen was also confirmed. This is possibly due to sealing issues in the thermal system and not being pressurized. The HIP system being pressurized can make it more difficult for the nitrogen to react with the titanium in addition to competing with the more reactive oxygen atoms.

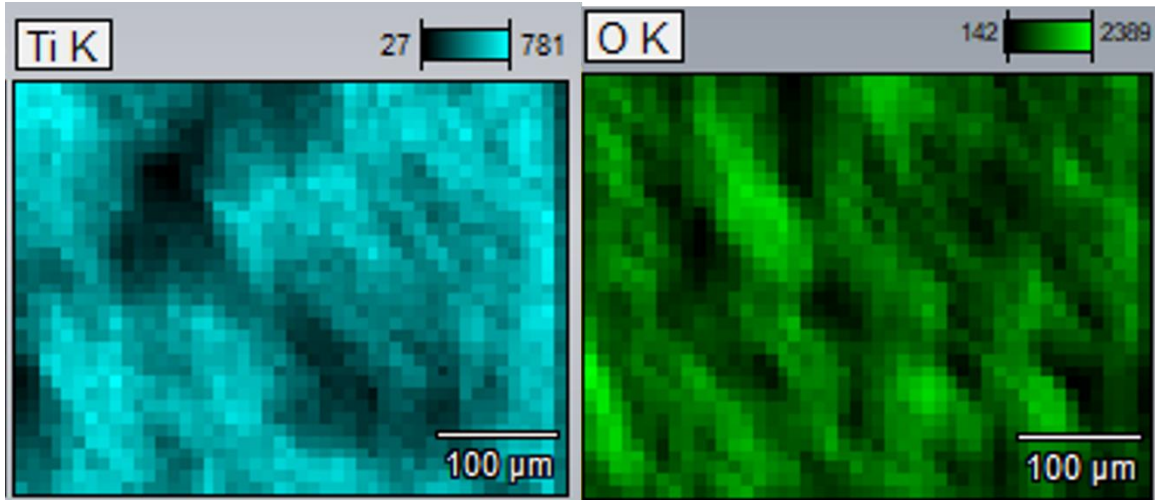


Figure 55. EDS mapping of the thermal sintered N<sub>2</sub> specimen.

The EDS map of the thermal sintered nitrogen is obtained and shown in Figure 55. Unlike the other test specimen, titanium and oxygen are only detectable on the surface. Oxygen is the dominant element over titanium. This is caused by the high affinity oxygen has for titanium to produce titanium oxide. The specimen was exposed to air on the cool down period and the oxide reaction overtook the nitride reaction on the surface.

### 6.3 Electrical Properties

Table 4. Electrical Properties of AM specimen vs. baseline BPP

Component	Area Specific Resistance (Ohm cm)	Target (<0.01 Ohm cm)	Electrical Conductivity (S/cm)	Target (>100 S/cm)
Bipolar Plate	0.179	Fail	5.59	Fail
HIP Cube	0.008	<b>Pass</b>	131.93	<b>Pass</b>
Sintered in Ar	.0007	<b>Pass</b>	1529.05	<b>Pass</b>
Sintered in N <sub>2</sub>	0.0169	Fail	59.17	Fail

The electrical properties of the AM specimen and the baseline BPP are shown in Table 4. The baseline BPP had the highest resistance. This is possibly due to the gradient apparent in the topography shown in Figure 51 and Figure 52. The combination of a smooth surface and a graded surface leads to lesser contact points at metal-to-metal interfaces. The thermal sintered N<sub>2</sub> sample with the higher oxide layer resulted in an increased resistance compared to the thermal sintered Ar slightly disqualifying it from reaching the target for area specific resistance and electrical conductivity. A thinner oxide layer will benefit the thermal sintered N<sub>2</sub> sample in an electrical capacity. The HIP cube and the thermal sintered Ar were able to meet the electrical targets.

#### 6.4 Corrosion Resistance

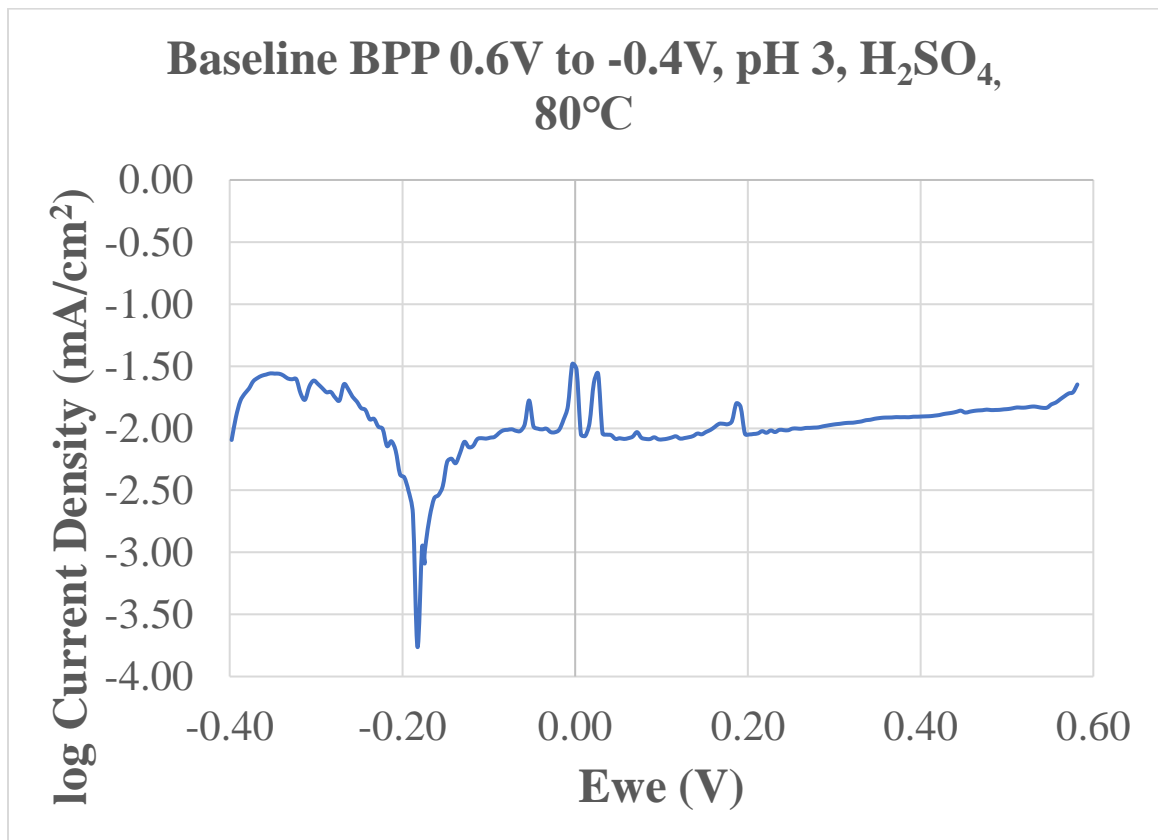


Figure 56. Tafel plot of the baseline BPP vs Ag/AgCl reference

The corrosion potential and the corrosion current density has been captured for the baseline BPP as shown in Figure 56. The open circuit corrosion potential was measured at 189.236 mV vs Ag/AgCl reference while the corresponding corrosion current density is given as 5.517 uA/cm<sup>2</sup>. This value is greater than the DOE target for corrosion current.

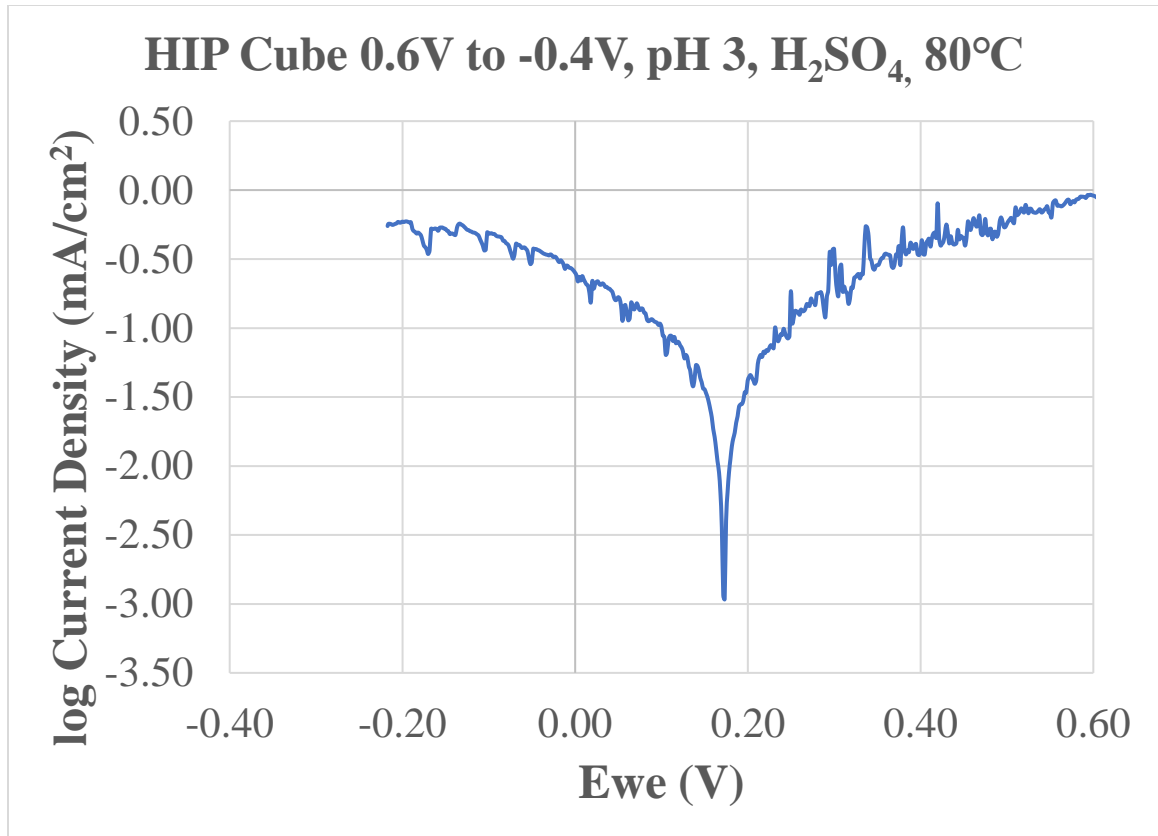


Figure 57. Tafel plot of the HIP cube vs Ag/AgCl reference.

The corrosion potential and the corrosion current density has been captured for the HIP cube as shown in Figure 57. The open circuit corrosion potential was measured at 172.338 mV vs Ag/AgCl reference while the corresponding corrosion current density is given as 108.751 uA/ cm<sup>2</sup>. This value supersedes the DOE target for corrosion. The fluctuations captured at the top of the curve is due to porosity. It is indicative of a modulating active surface area. The increased corrosion density is attribute to the activation of crevice corrosion from the rampant porosity. Crevice

corrosion increases current due the local increases of electrolyte concentration at smaller surface areas.

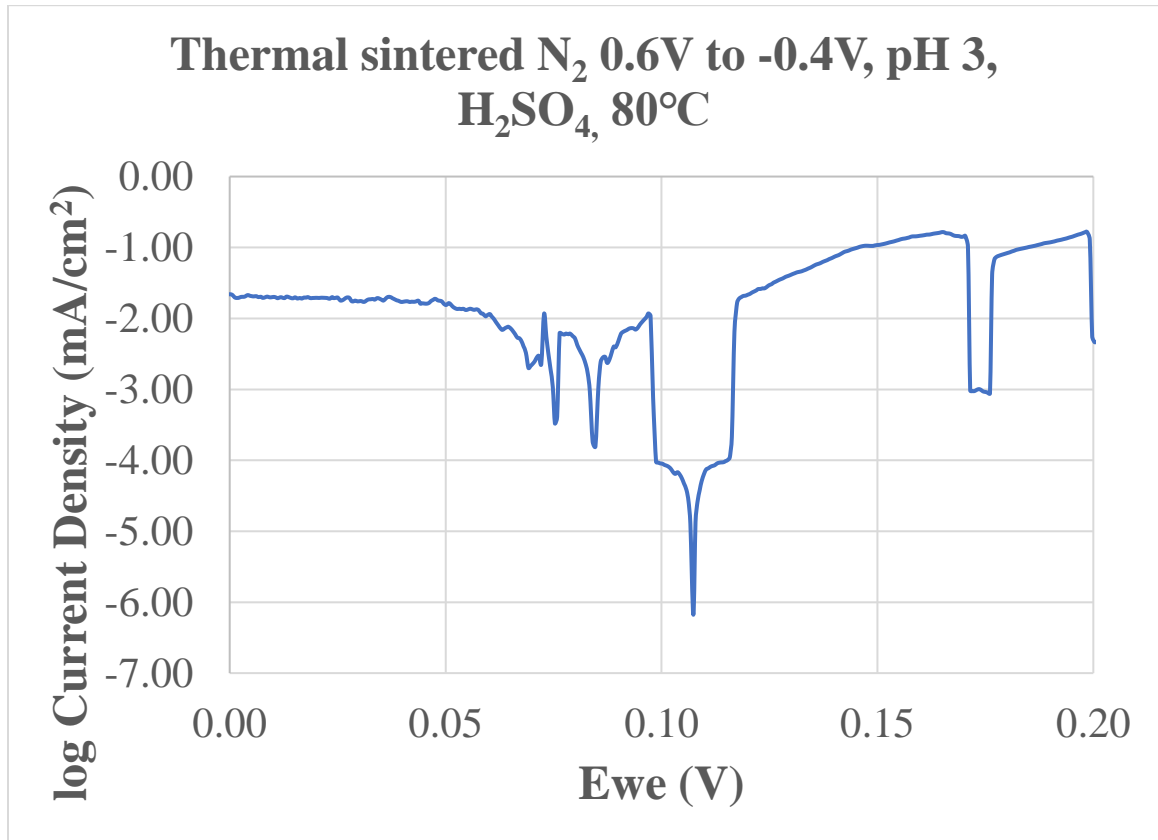


Figure 58. Tafel plot of the specimen thermal sintered in N<sub>2</sub> vs Ag/AgCl reference.

The corrosion potential and corrosion density has been captured for the thermal sintered N<sub>2</sub> specimen as shown in Figure 58. The open circuit potential was measured at 107.338 mV and the corresponding current density is 0.004 uA/ cm<sup>2</sup>. This value is sufficient for the DOE target. The fluctuations apparent in the plot surrounding the corrosion current spike is due to the refreshing of the electrolyte to maintain surface area coverage. The passivated layer from the sintering process provided corrosion protection allowing the sample to be well under the current density limit.

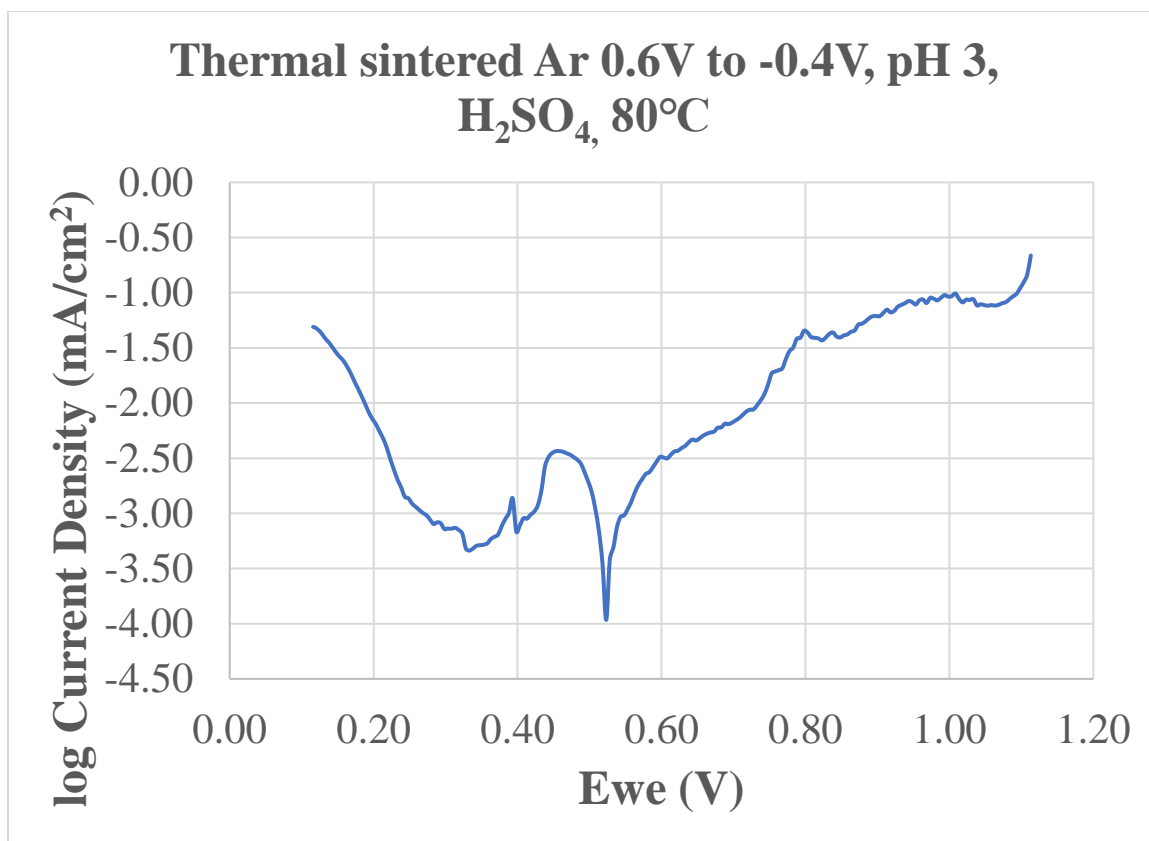


Figure 59. Tafel plot of the thermal sintered Ar specimen vs Ag/AgCl reference.

The corrosion potential and corrosion current density have been obtained for the thermal sintered Ar specimen as shown in Figure 59. The open circuit potential was measured at 509.122 mV vs Ag/AgCl reference with a corresponding current density of 0.358 uA/ cm<sup>2</sup>. Similar to the thermal sintered N<sub>2</sub>, the current density is sufficient for the target. The thermal sintering in argon provides an oxide and nitride presence. The control of the oxygen allows the nitrogen to react with the titanium in a balanced manner. The anodic and cathodic regions surrounding the corrosion current also experienced fluctuations due to the refreshing of the electrolyte to maintain area coverage. The current densities and pass/fail status for each sample is shown in Table 5.

Table 5. Current densities of test specimen from corrosion testing.

<b>Component</b>	<b>Current Density (<math>\mu\text{A}/\text{cm}^2</math>)</b>	<b>Target (&lt;1)</b>
Bipolar Plate	5.517	Fail
HIP Cube	108.751	Fail
Sinterface Ar	0.358	Pass
Sinterface N <sub>2</sub>	0.004	Pass

## 6.5 Hardness Testing

Table 6. Rockwell Hardness B of test specimen before and after thermal sintered in argon.

Wrought Ti-Grade 2 [55]	As Printed	Thermal sintered Ar	Thermal sintered N <sub>2</sub>
80	52.9	69.1	Fail
-	55.8	56.1	Fail
-	56.3	44.5	Fail
-	55.1	77.8	Fail

The hardness values obtained from the pre and post processed material show that when the AM titanium parts are sintered in argon, the conventional mechanical properties can be maintained. The decreased hardness for the argon sintered specimen is due to local porosity. Contrarily, the specimen sintered in nitrogen and air are too brittle. That defect coupled with the inherent porosity causes the samples to crumble at the onset of indentation preloading, therefore values were not obtained. It is observed that resolving the porosity due to low metal content and particle size will allow for the argon sintered material to undertake an oxide layer to enhance to corrosion resistance without sacrificing the structural integrity of the BPP. The obtained hardness results are shown in Table 6.

## 6.6 Summarize

In summary, the test specimens have been characterized according to the desirable properties for BPPs. The thermal sintered specimen both meet the target for corrosion resistance

while the thermal sintered argon and HIP cube meet the target for electrical conductivity. The thermal sintered N<sub>2</sub> produced the best corrosion resistance due to the increase oxide thickness.

## CHAPTER 7. CONCLUSIONS/FUTURE WORKS

### 7.1 Conclusions

In conclusion, the obtained results for the BPP characterization of the commercial filament can meet the standard of the 2030 DOE targets with the proper thermal process. The AM process has showed much promise to advance the development of BPP systems by implementing a new composite material with in-situ surface treatment possibilities. The key takeaways are:

- Titanium can be sintered and maintain wrought mechanical properties.
- Tunable oxide layer growth is possible using metal composite material and controlled atmospheres.
- Novel technique was implemented to accomplish the post processing.

### 7.2 Future Work

In the future, a feedstock filament with higher metal loading >80% vol and consistent particle size is necessary. This will help reduce the porosity that diminishes the direct applicability of the material. Also, a mass flow control system integrated into the furnace will provide more control of the atmosphere particularly in the development of the controlled oxide growth or any type of layered or sequential processing. This will be important to developing multi-layered BPP systems suitable for PEFC environments while taking advantage of passive geometry capabilities in AM. Future atmospheres to consider in addition to argon and nitrogen are carbon monoxide and reformat gas with low hydrogen concentrations. An important factor to perfecting the sintering for PEFC applications is in the control of the atmosphere.

### 7.3 Alternative Topics

The findings from this work do not have to be purely AM based. There can be a hybrid approach which is already common in manufacturing environments, i.e., using material extrusion to make test jigs or molds for traditional manufacturing processes. The AM material can be used to encase or embed a conventional substrate then perform the processing on the 3D printed layers.

## REFERENCES

- [1] F. Babir, PEM Fuel Cells: Theory and Practice, Amsterdam: Academic Press, 2012.
- [2] Sauermoser et. al, “Flowfield Patterns for PEMFCs”, Frontiers in Energy Research, Vol 8, 2020.
- [3] A. Alaswad, A. Omran, J. Sofre, T. Wilberforce, G. Pignatelli, M. Dassisti, A. Baroutaji, J. Olabi, “Technical and commercial challenges of proton-exchange membrane fuel cells,” Energies 14, 144, 2021.
- [4] Y. Wang, D. Diaz, K. Chen, Z. Wang, and X. Adroher, “Materials, technological status, and fundamentals of PEM fuel cells- A review, Materials Today, pp. 178-203, 2020.
- [5] J. Scholta, B. Rohland, V. Trapp, and U. Focken, “Investigations on novel low-cost graphite composite bipolar plates, “Journal of Power Sources, pp. 231-234, 1999.
- [6] R. Makkus, A. Janssen, F. Bruijin, and R. Mallant, “Stainless steel for cost competitive bipolar plates in PEMFCs, “Journal of Power Sources, pp. 274-282, 2000.
- [7] P. Rama, R. Chen, J. Andrews, “A review of performance degradation and failure modes for hydrogen fuelled polymer electrolyte fuel cells, Journal of Power and Energy, 222 (5), 2008.
- [8] Flex-Stak Open Bipolar Graphite Plate ([fuelcellstore.com](http://fuelcellstore.com))
- [9] T. Fuller, “Proton Exchange Membrane Fuel Cells 9”, The Electrochemical Society, 2009.
- [10]. Y. Kuan, C. Ciou, M. Shen, C. Wang, R. Fitrani, C. Lee, “Bipolar plate design and fabrication using graphite reinforced composite laminate for PEMFC”, International Journal of Hydrogen Energy, 46 (31), pp. 16801-16814,2021.
- [11]. S. Radhakrishnan, B. Ramanujam, A. Adhikari, S. Sivaram, “High-temperature polymer-graphite hybrid composites for bipolar plates: effect of processing conditions on electrical properties”, Journal of Power Sources, 163 (2), pp. 702-702, 2007.
- [12]. Q. Yin, A. Li, W. Wang, L. Xia, Y. Wang, “Study on the electrical and mechanical properties of phenol-formaldehyde resin/graphite composite for bipolar plate”, Journal of Power Sources, 165 (2), pp. 717-721, 2007.
- [13] A. Heinzl, F. Mahlendorf, O. Niemzig, C. Kreuz, “Injection moulded low-cost bipolar plates for PEM fuel cells” Journal of Power Sources, 2004.
- [14] A. Muller, P. Kauranen, A. Ganski, B. Hell, “Injection moulding of graphite composite bipolar plates”, Journal of Power Sources, 2006.
- [15] F. Mighri, M. Huneault, “Electrically conductive thermoplastic blends for injection and compression molding of bipolar plates in the fuel cell application”, Polymer Engineering and Science 44 (9), pp. 1755-1765, 2004.

- [16] <https://www.dana.com/product/composite-bipolar-plates/>
- [17] P. Hamilton, B. Pollet, "Fuel Cells", 10 (4), pp. 489-509, 2010.
- [18] H. Tawfik, Y. Hung, D. Mahajan, "Metal bipolar plates for PEM fuel cell: a review", Journal of Power Sources, 163 (2) 2007.
- [19] J. Scherer, D. Munter, R. Strobel, "Influence of metallic bipolar plates on the durability of polymer electrolyte fuel cells" Polymer Electrolyte Fuel Cell Durability, pp. 243-256, 2009.
- [20] T. Ous, C. Arcoumanis, "Degradation aspects of water formation and transport in proton exchange membrane fuel cell: a review", Journal of Power Sources, 240, pp. 558-582, 2013.
- [21] F. Silva, O. Ramirez, M. Tunes, P. Edmondson, J. Sagas, L. Fontana, H. Melo, C. Schon, "Corrosion resistance of functionally graded TiN/Ti coatings for proton exchange membrane fuel cells", International Journal of Hydrogen Energy, 45 (58), pp. 33993-34010, 2020.
- [22] F. Madadi, A. Rezaeian, H. Edris, M. Zhiani, "Improving performance in polymer electrolyte membrane fuel cell by applying different coatings to metallic bipolar plates", Materials Chemistry and Physics, 2019.
- [23] S. Jannat, H. Rashtchi, M., Atapour, M. Golozar, H. Elmkhah, M. Zhiani, "Preparation and performance of nanometric Ti/TiN multi-layer physical vapor deposited coating on 316L stainless steel as bipolar plate for proton exchange membrane fuel cells, "Journal of Power Sources, 2019.
- [24] P. Gao, Z. Xie, X. Wu, C. Ouyang, T. Lei, P. Yang, C. Liu, J. Wang, T. Ouyang, Q. Huang, "Development of Ti bipolar plates with carbon/PTFE/TiN-composite coating for PEMFCs", International Journal of Hydrogen Energy, 2018.
- [25] S. Lee, C. Huang, Y. Chen, "Investigation of PVD coating on corrosion resistance of metallic bipolar plates in PEM fuel cell, "Journal of Materials Processing, pp. 688-693, 2003.
- [26] Y. Song, C. Zhang, C. Ling, M. Han, R. Yong, D. Sun, J. Chen, "Review on current research of materials, fabrication and application for bipolar plate in proton exchange membrane fuel cell" International Journal of Hydrogen Energy, pp. 29832-29847, 2020.
- [27] Z. Sadeghian, M. Hadidi, D. Salehzadeh, A. Nemati, "Hydrophobic-octadecylamine functionalized graphene/TiO<sub>2</sub> hybrid coating for corrosion protection of copper bipolar plates in simulated proton exchange membrane fuel cell environment", International Journal of Hydrogen Energy, pp. 15380-15389, 2020.
- [28] J. Shi, P. Zhang, Y. Han, H. Wang, X. Wang, Y. Y, J. Sun, "Investigation on electrochemical behavior and surface conductivity of titanium carbide modified Ti bipolar plate of PEMFC", International Journal of Hydrogen Energy, pp. 10050-10058, 2020.

- [29] J. Wang, L. Min, F. Fang, W. Zhang, Y. Wang, "Electrodeposition of graphene nano-thick coating for highly enhanced performance of titanium bipolar plates in fuel cells," *International Journal of Hydrogen Energy*, pp. 16909-16917, 2019.
- [30] P. Zhang, C. Hao, F. Du, H. Wang, X. Wang, J. Sun, "Electrochemical behavior and surface conductivity of NbC modified Ti bipolar plate for proton exchange membrane fuel cell", *Surface and Coatings Technology*, 2020.
- [31] R. He, J. Jiang, R. Wang, Y. Yue, Y. Chen, T. Pan, "Anti-corrosion and conductivity of titanium diboride coating on metallic bipolar plates," *Corrosion Science*, 2020.
- [32] S. Wang, J. Peng, W. Lui, "Surface modification and development of titanium bipolar plates for PEM fuel cells," *Journal of Power Sources*, pp. 485-489, 2006.
- [33] N. Asri, T. Husaini, A. Sulong, E. Maijlan, W Daud, "Coating of stainless steel and titanium bipolar plates for anticorrosion in PEMFC: a review," *International Journal of Hydrogen Energy*, pp.9135-9148, 2017.
- [34] P. Lettenmeier, R. Wang, R. Aboutallah, B. Saruhan, O. Freitag, P. Gazdzicki, T. Morawietz, R. Hiesgen, A. Gago, K. Friedrich," Low-cost and durable bipolar plates for proton exchange membrane electrolyzers" *Scientific Reports*, 7, 2017.
- [35] R. Dawson, A. Patel, A. Rennie, S. White, "The use of additive manufacturing for metallic bipolar plates in PEEFC stacks," *Chemical Engineering Transactions*, 41, p. 175, 2014.
- [36] D. Bourell, W. Frazier, H. Kuhn, M. Seifi, "ASM Handbook: Additive Manufacturing Processes", ASM International, 2020.
- [37] F. Azam, A. Rani, K. Altaf, H. Zaharin, "An in-depth review on direct additive manufacturing of metals," *IOP Conference Series Materials Science and Engineering*, 328 (1), 2017.
- [38] D. Nguyen, H. Park, C. Lee, "Applying selective laser melting to join Al and Fe: an investigation of dissimilar materials," *Applied Science*, 9 (15), 2019.
- [39] S. Sing, C. Tey, W. Yeong, "3D printing of metals in rapid prototyping of biomaterials: techniques in additive manufacturing", *Biomaterials Second Edition*, 2020.
- [40] A. Klien, J. Clayton, "Developing an effective metal powder specification for binder jet additive manufacturing," *Metal Additive Manufacturing* 5 (2), 2019.
- [41] R. Mahamood, T. Jen, S. Akinlabi, S. Hassan, K. Abdulrahman, E. Akinlabi, "Role of additive manufacturing in the era of industry 4.0" *Additive Manufacturing*, pp. 107-126, 2021.
- [42] R. German, "Chapter 4: Measurement tools and experimental observations," *Sintering: from Empirical Observations to Scientific Principles*, pp. 71-130, 2014.

- [43] D. Heaney, "Vacuum sintering," *Sintering of Advanced Materials*, pp. 189-221, 2010.
- [44] R. German, "Chapter 15: Sintering practice," *Sintering: from Empirical Observations to scientific Principles*, pp. 471-512, 2014.
- [45] R. Speaker, R. Osterreich, S. Kazi, J. Buonassisi, "Sintering atmosphere analysis: selection and use of analyzers to monitor and control sintering atmospheres," *Advances in Powder Metallurgy and Particulate Materials*, pp. 16-31, 2003.
- [46] R. German, "Chapter 11: Mixed powders and composites," *Sintering: from Empirical Observations to Scientific Principles*, pp. 355-385, 2014.
- [47] X. Peng, L. Kong, J. Fuh, H. Wang, "A review of post-processing technologies in additive manufacturing," *Journal of Manufacturing and Materials Processing*, 5 (38), 2021.
- [48] A. Bose, C. Schuh, J. Tobia, N. Tuncer, N. Mykulowycz, A. Preston, A. Barbati, B. Kernan, M. Gibson, D. Krause, T. Brzezinski, J. Schroers, R. Fulop, J. Myerberg, M. Sowerbutts, Y. Chiang, A. Hart, E. Sachs, E. Lomeli, A. Lund, "Traditional and additive manufacturing of a new tungsten heavy alloy alternative," *International Journal of Refractory Metals and Hard Materials*, 73, pp. 22-28, 2018.
- [49] F. Froes, "Applications of titanium," in *Titanium Physical Metallurgy Processing and Applications*, Materials Park, ASM International, pp. 353-379, 2015.
- [50] M. Donachie, "Chapter 2: Introduction to selection of titanium alloys," in *Titanium: A Technical Guide 2nd Edition*, Materials Park, ASM International, pp. 5-13, 2000.
- [51] G. Lutjering, J. Williams, "Chapter 2: Fundamental aspects," in *Titanium*, Berlin, Springer, pp. 15-50, 2003.
- [52] <https://shop.thevirtualfoundry.com/collections/metal-filaments/products/titanium-alloy>
- [53] <https://aiphp.com/wp-content/uploads/2013/07/AIP-research-HIPs.pdf>
- [54] <https://www.gamry.com/basics-of-electrochemical-corrosion-measurements/>
- [55] "DOE Technical Targets for Polymer Electrolyte Membrane Fuel Cell Components," 5 January 2021. [Online]. Available: <https://www.energy.gov/eere/fuelcells/doe-technical-targets-polymer-electrolyte-membrane-fuel-cell-components>.
- [56] <https://asm.matweb.com/search/SpecificMaterial.asp?bassnum=MTU020>
- [57] <https://www.ge.com/additive/additive-manufacturing/machines/ebm-machines/arcam-ebm-spectra-h>

[58] <https://www.desktopmetal.com/products/shop>

[59] [https://www.trumpf.com/en\\_INT/products/machines-systems/additive-production-systems/truprint-1000/](https://www.trumpf.com/en_INT/products/machines-systems/additive-production-systems/truprint-1000/)

[60] <https://moneyinc.com/the-five-most-expensive-3d-printers-on-the-market-today/>

## VITA

David Alexander IV attended Tuskegee University and obtained a Bachelor of Science and Master of Science in Mechanical Engineering. He joined Los Alamos National Laboratory in 2018 as a Post Master's researcher. The following year David enrolled at the University of Texas at El Paso and graduated with his PhD. in Mechanical Engineering May 15<sup>th</sup>, 2022. David is an R&D Engineer 2 with the non-destructive testing and evaluation group at Los Alamos National Laboratory.